

# NH<sub>3</sub> and HNO<sub>x</sub> Formation and Loss in Nitrogen Fixation from Air with Water Vapor by Nonequilibrium Plasma

*Elise Vervloessem<sup>†,‡,\*</sup>, Mikhail Gromov<sup>‡,†</sup>, Nathalie De Geyter<sup>‡</sup>, Annemie Bogaerts<sup>†</sup>, Yury  
Gorbanev<sup>†,×</sup>, Anton Nikiforov<sup>‡,×</sup>*

<sup>†</sup>Research group PLASMANT, Department of Chemistry, University of Antwerp,  
Universiteitsplein 1, 2610 Wilrijk, Belgium

<sup>‡</sup>Research Unit Plasma Technology (RUPT), Department of Applied Physics, Ghent University,  
Sint-Pietersnieuwstraat 41, 9000 Ghent, Belgium

<sup>†</sup>Chimie des Interactions Plasma Surface (ChiPS), CIRMAP, Mons University, 20 Place du Parc,  
7000 Mons, Belgium

KEYWORDS Nitrogen fixation; ammonia; ammonium nitrite; nonequilibrium plasma; water  
vapor; optical emission spectroscopy

## ABSTRACT

The current global energy crisis indicated that increasing our insight into non-fossil fuel nitrogen fixation pathways for synthetic fertilizer production is more crucial than ever. Nonequilibrium plasma is a good candidate because it can use  $N_2$  or air as a N source, and water directly as a H source, instead of  $H_2$  or fossil fuel ( $CH_4$ ). In this work, we investigate  $NH_3$  gas phase formation pathways from humid  $N_2$  and especially humid air up to 2.4 mol%  $H_2O$  (100% relative humidity at 20 °C) by optical emission spectroscopy and Fourier-transform infrared spectroscopy. We demonstrate that the nitrogen fixation capacity is increased when water vapor is added, as this enables  $HNO_2$  and  $NH_3$  production in both  $N_2$  and air. However, we identified a significant loss mechanism for  $NH_3$  and  $HNO_2$  that occurs in systems where these species are synthesized simultaneously, i.e., downstream from the plasma,  $HNO_2$  reacts with  $NH_3$  to form  $NH_4NO_2$ , which rapidly decomposes into  $N_2$  and  $H_2O$ . We also discuss approaches to prevent this loss mechanism, as it reduces the effective nitrogen fixation when not properly addressed, and therefore should be considered in future works aimed at optimizing plasma-based  $N_2$  fixation. In-line removal of  $HNO_2$  or direct solvation in liquid are two proposed strategies to suppress this loss mechanism. Indeed, using liquid  $H_2O$  is beneficial for accumulation of the  $N_2$  fixation products. Finally, in humid air we also produce  $NH_4NO_3$ , from the reaction of  $HNO_3$  with  $NH_3$ , which is of direct interest for fertilizer application.

## INTRODUCTION

Since the invention of synthetic fertilizers, food production increased drastically and enabled mass population expansion.<sup>1</sup> The most important industrial process in the field of nitrogen fixation (NF) (for, among others, synthetic fertilizer production) is the Haber-Bosh (HB) process: a thermo-catalytic conversion of  $N_2$  and  $H_2$  into ammonia.<sup>2</sup> While supporting 50% of the world's

population<sup>3</sup>, the HB process depends on fossil fuels for energy and, for the majority of HB chemical plants, as the hydrogen source<sup>4,5</sup> as well. The HB process has been extensively optimized during its 100-year existence, and there is currently no viable alternative or complementary process bringing the same support.<sup>6</sup>

Because of the vital role synthetic fertilizers play and their accompanying high burden on the environment, it is of pivotal importance to research alternative ways for NF to ensure continuous improvement of synthetic fertilizer production. Although these alternative ways cannot fully substitute HB, they can present an appealing auxiliary technology of NF, especially in remote areas with abundant renewable electricity.<sup>7</sup> Moreover, because of the harsh conditions (high temperature and extreme pressure) required for its operation, HB is only economically feasible on large scales<sup>8</sup>, resulting in massive centralized production and subsequent costly distribution of the produced  $\text{NH}_3$ .

Plasma-based NF is therefore an interesting method to consider as an alternative, because it is electricity-based and can use abundant feedstock like air, nitrogen, and water.<sup>9,10</sup> The process is decentralized, can operate on a scale which would fit the very local demand, and is operated at atmospheric pressure, resulting in an overall environmentally and economically friendly local small-scale production, which also eliminates transportation costs.

Plasma is an ionized gas, comprised of electrons, photons, atoms, radicals, ions, and excited species. A variety of plasma sources and feed gases ( $\text{N}_2/\text{O}_2/\text{H}_2/\text{H}_2\text{O}$  combinations) have been reported for plasma-based NF into  $\text{NO}_x$ <sup>11-15</sup> and  $\text{NH}_3$  (in plasma-catalytic<sup>16,17</sup> and plasma-liquid<sup>18</sup> systems). A schematic overview is presented in Figure S1. Most of the reported plasma-based  $\text{NH}_3$  production methods rely on  $\text{H}_2$ , often in the presence of a catalyst.<sup>16,17</sup> Although  $\text{H}_2$  can be produced from water via electrolysis, a direct usage of water as a hydrogen source is of interest

for NH<sub>3</sub> production.<sup>10,19</sup> Therefore, studies of NH<sub>3</sub> formation and accumulation in plasma-treated water (PTW)<sup>20-24</sup>, sometimes coupled to another technology – a UV source, an ozonator<sup>25-27</sup> and/or an electrochemical cell<sup>28-30</sup> – have been gaining increased interest from both the scientific community and industry. Most of the advances in plasma-based nitrogen fixation are summarized in recent reviews.<sup>10,31</sup>

We have previously shown that H<sub>2</sub>O can also be used for the production of NH<sub>3</sub> from mixtures of N<sub>2</sub> and water vapor, and even more interestingly, from air (N<sub>2</sub> and O<sub>2</sub>) and water vapor (i.e., humid air), with accumulation of the produced NH<sub>3</sub> in liquid water.<sup>32</sup> However, plasma-based studies that have looked at N<sub>2</sub>/H<sub>2</sub>O vapor and air/H<sub>2</sub>O vapor (i.e., without liquid water) are very scarce.<sup>32,33</sup> Hence, more insight into the gas phase formation of NH<sub>3</sub> with water vapor is needed, not least to understand how NH<sub>3</sub> production can be achieved in both N<sub>2</sub> and air plasma using H<sub>2</sub>O as a hydrogen source.

In air/H<sub>2</sub>O and N<sub>2</sub>/H<sub>2</sub>O mixtures, the formation of HNO<sub>x</sub> is also of interest. The majority of fertilizers are ammonium salts produced from NH<sub>3</sub> and its oxidation product HNO<sub>3</sub>, which is commercially synthesized through the Ostwald process using HB-made NH<sub>3</sub> as feedstock.<sup>10</sup> The direct synthesis of HNO<sub>x</sub> alongside NH<sub>3</sub> could therefore result in a more streamlined production process.<sup>34</sup>

This work studies the selectivity of plasma-based NF in air and N<sub>2</sub> discharges at a relative humidity up to 100% at 20 °C (room temperature), i.e. up to 2.4 mol% H<sub>2</sub>O. For this, we employed a pulsed plasma jet, which we previously used to study the underlying mechanisms responsible for the record-low energy consumption (EC) value in case of NO<sub>x</sub> generation from dry air<sup>35</sup>, ultimately yielding a very low overall EC for NH<sub>3</sub> production via plasma-formed NO<sub>x</sub> further catalytically reduced into NH<sub>3</sub>.<sup>36</sup> More importantly, we also used this plasma jet<sup>32</sup> to

demonstrate that the gaseous  $\text{H}_2\text{O}$  present in the plasma feed gas (and not the liquid  $\text{H}_2\text{O}$ ) plays the major role in NF, which was later also observed by Toth et al.<sup>37</sup> Moreover, we showed that both dissolved  $\text{NH}_4^+$  and  $\text{NO}_x^-$  were formed when  $\text{H}_2\text{O}$  vapor was added to the plasma feed gas ( $\text{N}_2$  or air). In the present work, we elaborate on this topic, investigating the fundamentals behind the one-step NF process from gaseous  $\text{N}_2/\text{air}$  and  $\text{H}_2\text{O}$  via gas phase diagnostics: Fourier-transform infrared spectroscopy (FTIR) and optical emission spectroscopy (OES), to elucidate the formation mechanisms of the  $\text{H}_2\text{O}$ -based  $\text{NH}_3$ .

## EXPERIMENTAL

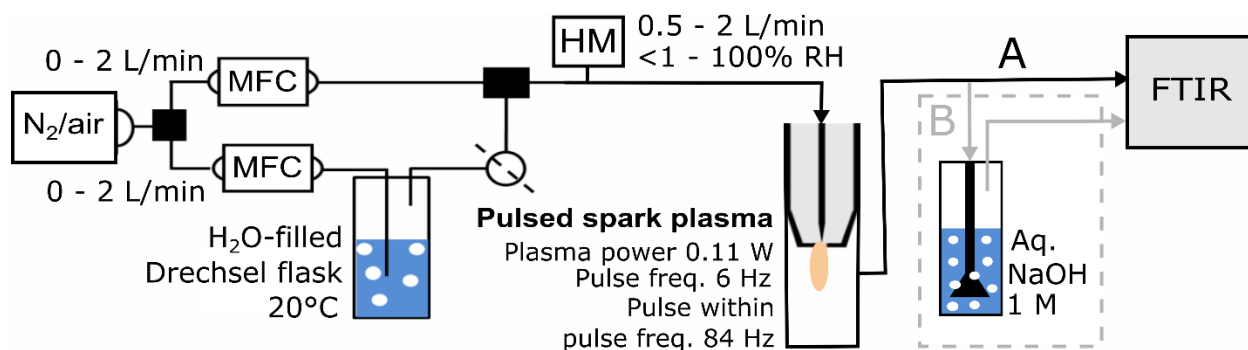


**Figure 1.** Experimental setup used in this work. Line A shows the setup where the effluent goes straight to the FTIR. Line B shows the setup where the effluent first passes a base washer, indicated in dashed grey. The latter is only used when specified in the text.

*Plasma setup.* A plasma jet operating in a pulsed spark mode was used, as shown in Figure S2, Supporting information (SI). The peak temperature in one pulse is  $1750 \pm 150$  K, however, the time-averaged temperature is ca. 315 K. Detailed characterization of this device can be found in our previous works.<sup>32,35</sup> Based on the V/I waveforms and discharge imaging, the operational mode of the discharge in both low and high humidity was a low current spark, which is generated in between the pin electrode and the nozzle.<sup>35</sup> The typical duration of the spark is in the range of

700 ns. Due to the nature of the discharge, its characteristics did not change strongly with different humidity levels, as shown elsewhere.<sup>32</sup> The plasma jet was operating either in synthetic air ( $\text{N}_2 + \text{O}_2$ ), or pure  $\text{N}_2$  (both  $\geq 99.999\%$ , Air Liquide). The gas flow rate was regulated using two mass flow controllers (MFCs; EL-Flow, Bronkhorst). Partial saturation of the supplied feed gas with  $\text{H}_2\text{O}$  vapor was achieved by splitting the main gas flow and passing its fraction through a water-filled bubbler.<sup>38,39</sup> The resulting gaseous  $\text{H}_2\text{O}$  concentration in the flow was monitored with a humidity meter (Testo 445). The feed gas flow rate was 0.5 or 2 Ls/min (standard liters per minute, henceforth referred to as L/min for simplicity). All tubing in the setup was Swagelok PTFE (diameter  $\frac{1}{4}$  inch). The concentration of  $\text{H}_2\text{O}$  vapor was varied, and will be shown in both molar percentage ( $<0.1$  to  $2.4$  mol%) and relative humidity at  $20$  °C ( $<1$  to  $100\%$ ). We explicitly note that even with no added  $\text{H}_2\text{O}$  vapor, the feed gas contained residual humidity, hence the absence of the zero value humidity. The effluent of the plasma jet was contained within a quartz reservoir (ca.  $30$  mL volume), the exhaust of which was connected to the FTIR spectrometer, as shown in Figure 1 (length ca.  $50$  cm).

*Downstream gas phase analysis.* N-containing stable gaseous products were measured employing FTIR (Matrix-MG2, Bruker,  $5$  m optical path, using an average of  $50$  scans, all gas from the setup plasma was directed to the FTIR). Quantitative measurements of  $\text{NO}$ ,  $\text{NO}_2$  and  $\text{N}_2\text{O}$  were performed using Bruker's database and Beer's law based on the absorption cross-sections from the HITRAN database<sup>40</sup> The deviation between methods was found to be  $<3\%$ . The concentration of gaseous  $\text{NH}_3$  and  $\text{HNO}_2$  were calculated through Beer's law only, using the absorbance cross-section reported by Barney et al..<sup>41</sup> Details on the experimental procedure and data processing can be found in SI, section S3, and Figure S3.

*OES analysis of the plasma-produced species.* The NO ( $A^2\Sigma^+-^2\Pi$ ; 226.94 nm), NH ( $A^3\Pi-X^3\Sigma$ ; 336.0 nm), and N<sub>2</sub> ( $C^3\Pi-B^3\Pi$ ; Second Positive System; 337 nm) transitions<sup>42</sup> were measured as shown in Figure S4 (section S4 of SI). We performed measurements (i) axially in the plasma (Figure S4a), as well (ii) space-resolved perpendicularly to the plasma effluent (Figure S4b) using (i) a Horiba iHR550 spectrometer with UV 250 nm blazed grating of 2400 g/mm and (ii) a Zolix Omni750 spectrometer with 500 nm blazed grating of 3600 g/mm equipped with a linear fiber optics array slit, respectively. In the axial position, the presented results were corrected for quenching by H<sub>2</sub>O, O<sub>2</sub> and N<sub>2</sub>, the sensitivity at different wavelengths, and the difference in the electron impact excitation coefficients for the NO( $A^2\Sigma^+$ ) and NH( $A^3\Pi$ ) states. This means that the intensities of NO( $A^2\Sigma^+$ ) and NH( $A^3\Pi$ ) bands at different gas mixtures can be compared directly after the performed calculations, i.e. as a function of the humidity. The measured intensities can be correlated to ground state NH and NO densities when assuming that excitation to these states occurs predominantly through electron impact. This approach is based on the following approximations (similar to corona approximation<sup>43</sup>): (1) we do not consider collisional excitations, e.g. N<sub>2</sub>( $A^3\Sigma$ ) + NO  $\rightarrow$  N<sub>2</sub> + NO( $A^2\Sigma$ ); (2) the difference in excitation probability is calculated assuming a Maxwell electron energy distribution; (3) we do not consider de-excitation processes through V-V and V-T transfer and charge exchange. We infer that the corrections we made suffice to support the discussion of the obtained results.

The detailed description of the approach, including all computational corrections and normalization based on both experimental data and calculated values can be found in SI, Section S5, Table S1 and S2.

## RESULTS AND DISCUSSION

*Net production of NH<sub>3</sub>, NO<sub>x</sub> and HNO<sub>x</sub> downstream.* First, we studied the production of various stable compounds in the gas phase using FTIR, using the set-up shown in Figure 1, without base washer, hence following line A. Figure 2a and 2b show the NH<sub>3</sub> and HNO<sub>2</sub> concentration in N<sub>2</sub> at 0.5 L/min and 2 L/min gas flow rate. The results of similar experiments, but with humid air, are shown in Figure 2c and 2d, where besides NH<sub>3</sub> and HNO<sub>2</sub> also NO and NO<sub>2</sub> were detected. At all conditions tested, the N<sub>2</sub>O<sub>5</sub>, NO<sub>3</sub>, O<sub>3</sub> and HNO<sub>3</sub> concentrations were below the limit of detection. The highest observed N<sub>2</sub>O concentration did not exceed 2 ppm, and was thus considered negligible. An overview of the FTIR bands of interest is presented in Figure S3.

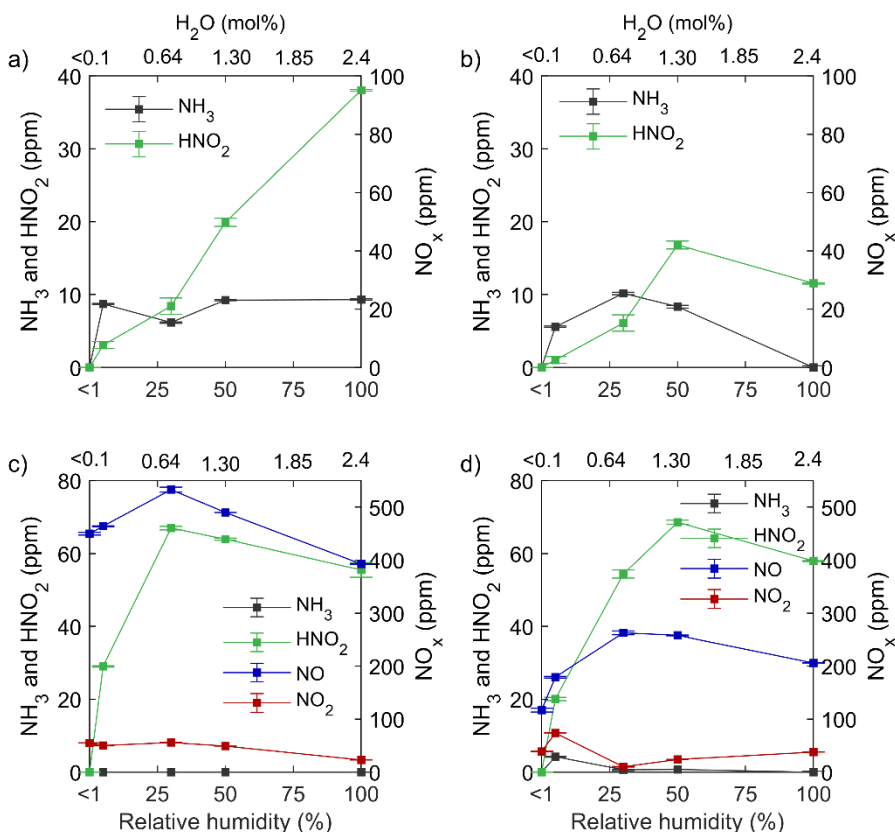




**Figure 2.** Concentration of  $\text{NH}_3$ ,  $\text{HNO}_2$  (left y-axis), and  $\text{NO}_x$  (right y-axis) in the gas phase as a function of feed gas humidity. (a)  $\text{N}_2$ , 0.5 L/min; (b)  $\text{N}_2$ , 2 L/min; (c) air, 0.5 L/min; (d) air, 2 L/min.

In this discussion, we focus on the possible pathways of nitrogen fixation, leading to the production of  $\text{HNO}_2$ ,  $\text{HNO}_3$ , and  $\text{NH}_3$ . A discussion on the  $\text{NO}$  and  $\text{NO}_2$  production and their interplay with water can be found in the SI.

As a common trend in both humid  $\text{N}_2$  and humid air, when the  $\text{H}_2\text{O}$  content of the feed gas increases, the  $\text{HNO}_2$  concentration initially rises, as more H and O become available through  $\text{H}_2\text{O}$  dissociation into H atoms and OH radicals. In  $\text{N}_2$  feed gas, since  $\text{NO}$  is produced predominantly from OH (formed through water dissociation), we observe a continuous increase in  $\text{HNO}_2$  concentration with increasing humidity, for 0.5 L/min (Figure 2a), while at 2 L/min, a maximum is reached at 50% relative humidity (Figure 2b). In air, the highest  $\text{HNO}_2$  concentration (around 70 ppm) is measured between 25 and 50% relative humidity (Figure 2c and d). Note that the chemistry of the system becomes more complex in humid air compared to humid  $\text{N}_2$ , rendering a detailed discussion on the mechanisms too speculative. However, a plausible hypothesis why in both  $\text{N}_2$  and air, instead of  $\text{HNO}_2$  rising until 100% humidity, its concentration decreases at higher  $\text{H}_2\text{O}$  vapor content (i.e., 50–100% for 2 L/min in air and  $\text{N}_2$ , and 25–100% for 0.5 L/min in air), will be given further down below.

Because  $\text{H}_2\text{O}$  is the sole H source in humid  $\text{N}_2$ , one could expect the  $\text{NH}_3$  concentration to rise with increasing  $\text{H}_2\text{O}$  vapor content as well. However, in the present study the gas phase  $\text{NH}_3$  concentration instead stays constant around 10 ppm at humidity above 5% ( $\text{N}_2$ , 0.5 L/min; Figure 2a) or even starts dropping after reaching a maximum of ca. 10 ppm at 25% humidity ( $\text{N}_2$ , 2

L/min; Figure 2b). At the same time, in air, despite being H<sub>2</sub>O present as an H source, no NH<sub>3</sub> is detected, except for one condition (air, 2 L/min, 5% humidity; Figure 2d). This is counterintuitive, because we previously observed NH<sub>3</sub> accumulation in liquid when the plasma effluent was placed above a water surface, and NH<sub>3</sub> was measured in PTW (as NH<sub>4</sub><sup>+</sup>).<sup>32</sup> Additionally, we confirmed in our previous work that most H in the formed NH<sub>3</sub> came from the gaseous H<sub>2</sub>O, with only a minor contribution of liquid H<sub>2</sub>O to the formation of NH<sub>3</sub>. This clearly indicated that NH<sub>3</sub> should be formed in the gas phase of the plasma system, although it is not detected by the downstream FTIR analysis in the present work.

Moreover, HNO<sub>3</sub> (detected in PTW as NO<sub>3</sub><sup>-</sup>) was not detected by FTIR in the gas phase under any of the conditions tested. We propose that the reasons are as follows. (i) Gaseous HNO<sub>3</sub> is mainly formed from NO<sub>2</sub> via reaction with OH<sup>36</sup> (see also Table 1 below), however NO<sub>2</sub> is not detected in humid N<sub>2</sub> (Figure 2a and b), and in humid air it is present in low concentrations (much lower than NO) (Figure 2c and d). Furthermore, (ii) we hypothesize the formation of NH<sub>4</sub>NO<sub>3</sub> and its precipitation out of the gas phase, as described by Zhu et al.<sup>44</sup> The latter hypothesis was supported by the observed accumulation of white dust during our experiments (see below). Still, we need an in-situ plasma gas phase analysis to elucidate the presence of NH<sub>x</sub> species created by the plasma from N<sub>2</sub> and H<sub>2</sub>O in both air and nitrogen feed gas, as shown below.

To investigate the near-simultaneous decrease of NH<sub>3</sub> and HNO<sub>2</sub> at high relative humidity (especially for humid N<sub>2</sub> at 2 L/min; Figure 2b), and the absence of detected NH<sub>3</sub> in air when switching from a humid gas-liquid system (as in our previous work<sup>32</sup>) to a pure humid gas system (Figure 2c and d), we studied the chemical species in the plasma and in the plasma afterglow by means of OES (Figure S4a and S4b). OES is a widely used analytical technique for

qualitative and quantitative plasma analysis. It measures the light emission from state transitions in a non-intrusive way, allowing qualitative insight into (short lived) species in the plasma itself and right after the plasma, before potential downstream reactions take place.<sup>45</sup>

*OES shows NH and NO are produced in the plasma.* First, we analysed the gas composition immediately inside the plasma. This was done by placing the OES spectrometer axially to the plasma jet (see Figure S4a).

The direct OES data provides the intensity of the signals related to the density of excited species. After the made corrections (described above and in the SI, section S5), we can correlate the intensity of the bands of the excited states  $\text{NH}(\text{A}^3\Pi)$  and  $\text{NO}(\text{A}^2\Sigma^+)$  to their ground state density taking into account the approximations behind the corona model applied. This means the resulting corrected data in Figure 3 are representative of the NH and NO ground state concentrations in the plasma. It has been shown that NH is predictive of and correlates with, the concentration of  $\text{NH}_3$ .<sup>46</sup> In (humid)  $\text{N}_2$  the trend of  $\text{NO}(\text{A}^2\Sigma^+)$  intensity follows the gas phase  $\text{HNO}_2$  concentration with increasing  $\text{H}_2\text{O}$  content, suggesting NO is directly involved in  $\text{HNO}_2$  formation (Figure 3a and 3b).

On the contrary, in (humid)  $\text{N}_2$ , the NH trend (based on the  $\text{NH}(\text{A}^3\Pi)$  intensity) and the  $\text{NH}_3$  trend (measured downstream) show opposite behavior at high humidity (50–100%  $\text{H}_2\text{O}$  content; see Figure 2a and 2b). I.e. inside the plasma the NH generation continues rising throughout the whole humidity range, corresponding to the increase in  $\text{H}_2\text{O}$  (and hence H), as shown in Figure 3a and 3b, while  $\text{NH}_3$  decreases or plateaus after 50% humidity. Most importantly, the results with (humid) air not only show the presence of  $\text{NH}(\text{A}^3\Pi)$ , but also its increase with increasing  $\text{H}_2\text{O}$  vapor content (Figure 3c and 3d), contrary to the lack of  $\text{NH}_3$  in the gas phase downstream

(see Figure 2c and 2d). This clearly demonstrates that the  $\text{NH}_3$  precursor  $\text{NH}$  is produced in the plasma, both in humid  $\text{N}_2$  and air. This discrepancy in the  $\text{NH}$  behavior compared to  $\text{NH}_3$  suggests that  $\text{NH}_3$  is “lost” after the plasma, before the downstream FTIR analysis. In order to obtain insights in the aforementioned pathway of  $\text{NH}_3$  decomposition, we used spatially resolved emission spectroscopy, perpendicularly to the plasma effluent (Figure S4b). For these conditions we also measured  $\text{N}_2(\text{C}^3\Pi\text{--B}^3\Pi)$  (see below), and found a correlation between  $\text{NO}$  and the excited state of  $\text{N}_2$ . Indeed, next to ground state and vibrationally excited  $\text{N}_2$ , electronically excited  $\text{N}_2$  also plays a role in the main formation reactions of  $\text{NO}$ , i.e. the Zeldovich mechanism (RS1 and RS2, in the SI).<sup>35</sup>

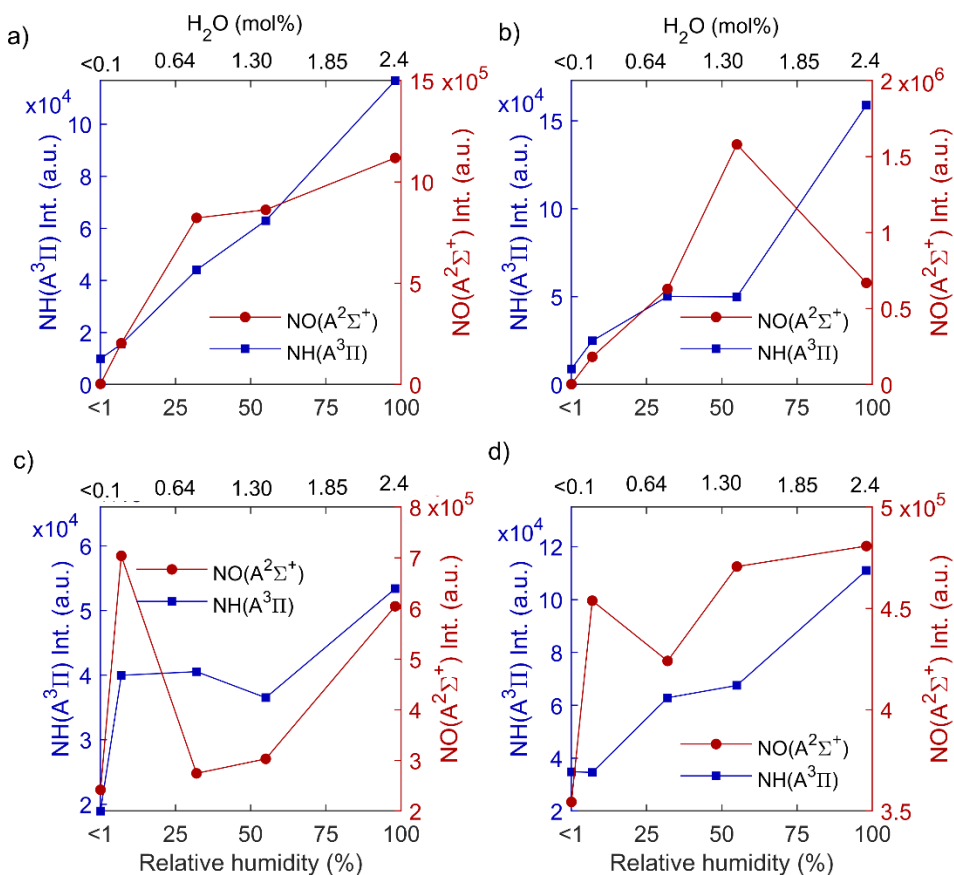


**Figure 3.** NH( $A^3\Pi$ ) (left y-axis) and NO( $A^2\Sigma^+$ ) (right y-axis) intensities in the plasma as a function of feed gas humidity. (a)  $N_2$ , 0.5 L/min; (b)  $N_2$ , 2 L/min; (c) air, 0.5 L/min; (d) air, 2 L/min.

*NH presence in the plasma afterglow.* In the afterglow, the following state transitions were observed: NH( $A^3\Pi-X^3\Sigma$ ),  $N_2(C^3\Pi-B^3\Pi)$  and NO( $B^2\Pi-X^2\Pi$ ). The NO( $A^2\Sigma^+-X^2\Pi$ ) transition was below the limit of detection in the afterglow under the conditions studied, however, the NO( $B^2\Pi-X^2\Pi$ ) transition is visible in the 338–340 nm region for some conditions. Figure 4 shows typical emission spectra (334–340 nm) along the plasma jet stream measured at the distance from 1 to 10 mm from the jet’s outlet (or nozzle), for 5% relative humidity in  $N_2$  and air, at 2 L/min. Spectra for all other conditions ( $N_2$  and air, 0.5 and 2 L/min, from <1 to 100% relative humidity) are found in Figure S5.

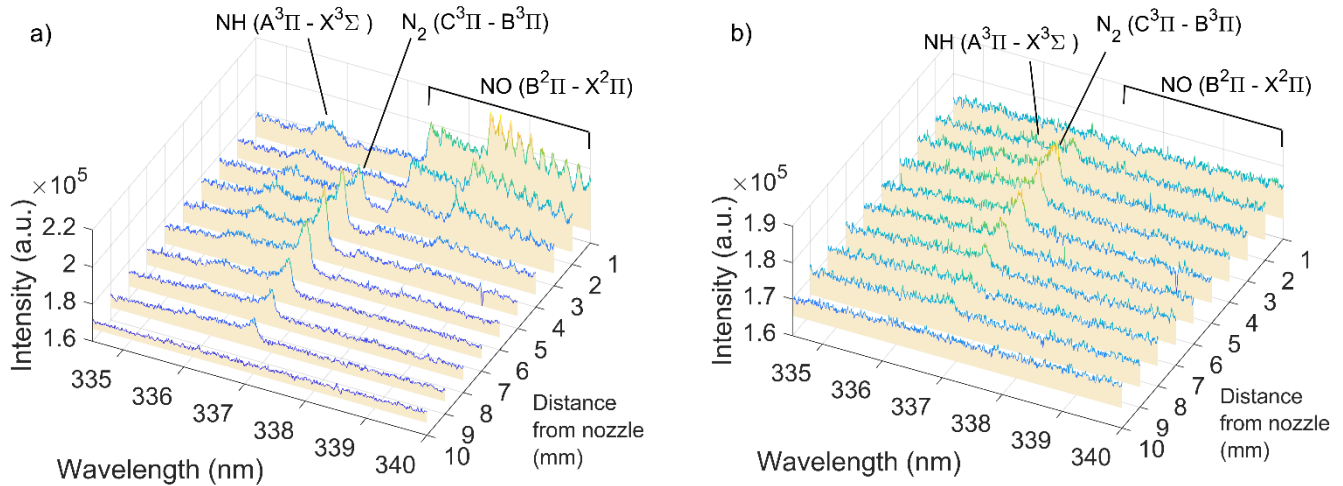


**Figure 4.** Emission spectra (334–340 nm) as a function of distance from the jet nozzle (1–10 mm), for 5% relative humidity at 2 L/min, in  $N_2$  (a) and air (b).

It is worth noting that  $N_2(C^3\Pi-B^3\Pi)$  was also observed in the axial OES. However, there its

presence is non-informative. In contrast, the space-resolved perpendicular OES allowed us to draw conclusions on the relationship between various chemical species present in the plasma afterglow.

While no direct correlation between  $\text{NO}(\text{B}^2\Pi\text{-X}^2\Pi)$  and either of the  $\text{NH}(\text{A}^3\Pi)$  and  $\text{N}_2(\text{C}^3\Pi)$  was found, the obtained data allowed us to draw conclusions on the relationship between  $\text{NH}(\text{A}^3\Pi)$  and  $\text{N}_2(\text{C}^3\Pi)$ . At all conditions,  $\text{NH}(\text{A}^3\Pi)$  correlates strongly with the presence of  $\text{N}_2(\text{C}^3\Pi)$  in the plasma and in the afterglow. Indeed, next to vibrationally excited  $\text{N}_2$ , electronically excited  $\text{N}_2$  also plays a role in the splitting of  $\text{N}_2$ , which is a necessary step in  $\text{NH}$  formation.<sup>35</sup>

Interestingly, at low humidity (5–30%) in  $\text{N}_2$ , another excited state,  $\text{N}_2(\text{B}^2\Pi)$ , is formed through high energy electrons, and is effectively quenched at higher  $\text{H}_2\text{O}$  concentrations and at higher  $\text{O}_2$  fractions.<sup>47</sup> This is the reason why the  $\text{NO}(\text{B}^2\Pi)$  emission is visible only in  $\text{N}_2$  gas, and only at low humidity (Figure 4a; see also Figure S5k, q and to a lesser extent l and r).  $\text{NH}(\text{A}^3\Pi)$  is observed in  $\text{N}_2$  even when only trace amounts of  $\text{H}_2\text{O}$  vapor are present (see Figure S5k and S4p in SI), due to the relatively low excitation energy needed for  $\text{NH}$  ground state excitation (3.68 eV)<sup>48</sup>, and because there is only a small amount of strong quenchers present (i.e.  $\text{H}_2\text{O}$ ) for  $\text{NH}(\text{A}^3\Pi)$ <sup>49,50</sup> in the feed gas.

As discussed above, no  $\text{NH}_3$  was detected in the gas phase downstream when humid air was used as feed gas. At the same time, we have measured  $\text{NH}_3$  in liquid when the plasma was placed above liquid water<sup>32</sup> and we observe by OES the formation of  $\text{NH}(\text{A}^3\Pi)$ , an indicator for  $\text{NH}_3$ , when humid air is used, both in the plasma and in the afterglow.

*$\text{NH}_3$  and  $\text{HNO}_x$  loss through salt formation and decomposition.* To explain this discrepancy, we considered that  $\text{NH}_3$  can form salts with  $\text{HNO}_x$  and looked at the most commonly reported

pathways for the formation and decomposition of  $\text{NH}_4\text{NO}_x$  (summarized in Table 1, R1-R8).<sup>51-</sup>

<sup>53</sup> It is known from selective catalytic reduction process (SCR) that  $\text{NO}_x$  and  $\text{HNO}_x$  can react with  $\text{NH}_3$ , which facilitates their conversion into  $\text{N}_2$  and  $\text{H}_2\text{O}$  via  $\text{NH}_4\text{NO}_2$  and  $\text{NH}_4\text{NO}_3$  intermediates. Unlike in SCR, in plasma synthesis, the formation of  $\text{NH}_4\text{NO}_2$  is undesirable as it decomposes back to  $\text{N}_2$  and  $\text{H}_2\text{O}$  at room temperature and atmospheric pressure.<sup>54</sup> On the other hand,  $\text{NH}_4\text{NO}_3$  is more stable and requires higher temperatures to undergo decomposition (R7).<sup>52,55,56</sup> The formation of  $\text{NH}_4\text{NO}_x$  has been observed in plasma systems as well, e.g. in a dielectric barrier discharge (DBD) plasmas which focus on  $\text{NH}_3$  oxidation.<sup>57,58</sup>

In our experimental setup, the residence time between the plasma and the FTIR (0.07 and 0.3 s for 2 and 0.5 L/min, respectively) is sufficient to allow complete conversion of  $\text{NH}_3$  and  $\text{HNO}_2$  into  $\text{NH}_4\text{NO}_2$  (assuming reaction R3). Indeed, the timescale for loss of  $\text{NH}_3$  (drop in concentration from 50 ppm to 0.1 ppm) would be around 0.1 s, making  $\text{NH}_4\text{NO}_2$  formation a plausible pathway in this system.

**Table 1.** Relevant reactions, and corresponding reaction rate coefficients and relevant temperature ranges, for the formation and decomposition of  $\text{NH}_4\text{NO}_x$ .

Reaction	Rate coefficient <sup>a</sup> /Equilibrium constant (R9) <sup>b</sup>	Temperature range	Ref
$\text{NO} + \text{OH} + \text{M} \rightarrow \text{HNO}_2 + \text{M}$	$7.52 \times 10^{-31} (\text{T}/300)^{-2.4}$	200–400 K	R1 <sup>59</sup>
$\text{NO}_2 + \text{OH} + \text{M} \rightarrow \text{HNO}_3 + \text{M}$	$1.63 \times 10^{-30} (\text{T}/300)^{-2.9}$	300–600 K	R2 <sup>60</sup>
$\text{HNO}_2 + \text{NH}_3 \rightarrow [\text{NH}_4\text{NO}_2]$	$3.65 \times 10^{-18}$	298 K	R3 <sup>61</sup>
$\text{HNO}_2 + \text{NH}_4\text{NO}_3 \rightarrow [\text{NH}_4\text{NO}_2] + \text{HNO}_3$	n/a		R4 <sup>53</sup>

$[\text{NH}_4\text{NO}_2] \rightarrow \text{N}_2 + 2\text{H}_2\text{O}$	n/a (unstable)	<400 K	R5	54
$\text{NH}_3(\text{g}) + \text{HNO}_3(\text{g}) \leftrightarrow \text{NH}_4\text{NO}_3(\text{s})$	$2.46 \times 10^{10} \times$ $(118.87 - 24084/T - 6.025 \times \ln(T))$	265–305 K	R6	62
$\text{NH}_4\text{NO}_3 \rightarrow \text{N}_2\text{O} + 2\text{H}_2\text{O}^c$	$10^{6.7} \times e^{-86/RT}, 10^{14} \times e^{-207/RT}$	350–600 K	R7	63
$\text{NH}_4\text{NO}_3 + \text{NO} \rightarrow \text{NO}_2 + \text{NH}_4\text{NO}_2$	n/a		R8	53,64

M is any neutral molecule and T is the gas temperature

<sup>a</sup> Unit:  $\text{cm}^3/(\text{molecules} \cdot \text{s})$  for two-body reactions, and  $\text{cm}^6/(\text{molecules}^2 \cdot \text{s})$  for three-body reactions.

<sup>b</sup> Unit:  $\text{molecules}^2/\text{cm}^6$

<sup>c</sup> In the temperature range 530 - 560 K, 98% of the irreversible decomposition of  $\text{NH}_4\text{NO}_3$  occurs via this reaction.<sup>65</sup> However, in NO rich conditions R8 is more favourable.<sup>53</sup>

Therefore, we hypothesize that downstream from the plasma in our system  $\text{HNO}_2$  reacts with  $\text{NH}_3$  to form  $\text{NH}_4\text{NO}_2$ , which rapidly decomposes into  $\text{N}_2$  and  $\text{H}_2\text{O}$  (R3-R5).<sup>55,66</sup> We note that  $\text{NH}_4\text{NO}_2$  can also be formed through  $\text{HNO}_3$  as an intermediate (R4). However, we assume this pathway to be negligible in our experiments because we observe  $\text{HNO}_3$  neither in the gas nor in the liquid.

Another plausible explanation is the precipitation of  $\text{NH}_4\text{NO}_3$ , which has also been described in SCR systems and as a direct product in plasma systems.<sup>52,55,56</sup> However, in the case of  $\text{N}_2$  as feed gas, formation of  $\text{NH}_4\text{NO}_3$  is unlikely: this would require  $\text{HNO}_3$  being present, but we detected  $\text{HNO}_3$  neither in the gas phase (this work) nor in PTW in our previous work.<sup>32</sup> Therefore, we infer that while in humid air plasma the loss of  $\text{NH}_3$  is possible through  $\text{NH}_4\text{NO}_3$  (R6, R7 and R8) and  $\text{NH}_4\text{NO}_2$  (R3, R4, R5 and R8), in  $\text{N}_2$  plasma the loss of  $\text{NH}_3$  at higher humidity levels, as seen in Figure 2a and 2b, occurs almost solely through  $\text{NH}_4\text{NO}_2$ .

To confirm our hypothesis about  $\text{NH}_4\text{NO}_x$ , we performed an in-line removal of  $\text{HNO}_2$  (and possibly  $\text{HNO}_3$ ) immediately after plasma by adding a Drechsel flask with 1M aqueous solution



of NaOH (see Figure 1, following line B, i.e. including the base washer). This basic medium completely dissolves gaseous  $\text{HNO}_x$ , while hindering the solvation of gaseous  $\text{NH}_3$  which thus passes further downstream, as was shown in the case of  $\text{N}_2$  with  $\text{H}_2\text{O}$  vapour.<sup>23</sup> Figure 5 shows the effect of  $\text{HNO}_x$  removal on the FTIR spectra, reflected in the  $\text{NH}_3$  concentration measured in the gas phase downstream from plasma. When an alkaline medium is added to trap  $\text{HNO}_2$ , the concentration of  $\text{NH}_3$  in humid air goes from non-detectable (cf. also Figure 2c and d) to clearly detectable (Figure 5). Specifically, at 2 L/min air, 100% RH, we measured  $\text{NH}_3$  concentration of ca. 50 ppm in the gas phase. This fully supports our above hypothesis.

Thus, we demonstrate for the first time that NF from air with  $\text{H}_2\text{O}$  vapor proceeds via a pathway towards  $\text{NH}_3$  as well as  $\text{NO}_x/\text{HNO}_x$ , but this can be overlooked because of the product loss downstream due to side reactions leading to  $\text{NH}_3$  decomposition.

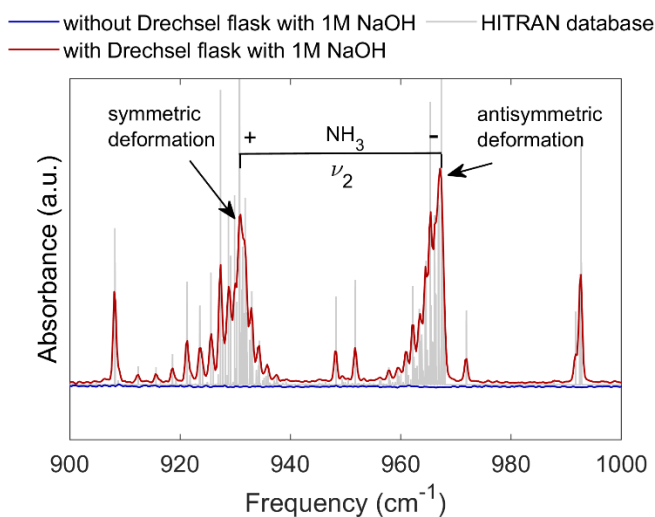


**Figure 5.** FTIR spectra of the  $\text{NH}_3$   $\nu_2$  deformation region, with and without  $\text{HNO}_x$  removal by NaOH, at 100% relative humidity in air, 2 L/min. The symmetric and antisymmetric deformations of  $\text{NH}_3$  are shown, together with the simulated  $\text{NH}_3$  spectrum in this range as obtained from the HITRAN database.<sup>67</sup>

These data are consistent with the drop in HNO<sub>2</sub> and NH<sub>3</sub> concentrations at a H<sub>2</sub>O content above 30% relative humidity (Figure 2). Once HNO<sub>2</sub> and NH<sub>3</sub> are produced simultaneously, NH<sub>4</sub>NO<sub>2</sub> starts being formed and further decomposes, thus effectively decreasing the net HNO<sub>2</sub> and NH<sub>3</sub> production. In air, the concentrations of the generated HNO<sub>x</sub> are certainly higher than in N<sub>2</sub>, due to the presence of O<sub>2</sub> and associated oxidative pathways. At the same time, in air the concentration of NH<sub>3</sub> is likely lower due to the larger contribution of competing reactions with the excited N<sub>2</sub> molecules (i.e., oxidative versus reductive NF). As a result, some (but not all) NH<sub>3</sub> and some HNO<sub>x</sub> are likely lost due to the NH<sub>4</sub>NO<sub>x</sub> formation when N<sub>2</sub> is the feed gas, while virtually all NH<sub>3</sub> is lost when using air.

This effect appears to be slightly different at 0.5 L/min in N<sub>2</sub> (Figure 2a). Even though the NH<sub>3</sub> concentration plateaus instead of rises upon increasing humidity, both HNO<sub>2</sub> and NH<sub>3</sub> do not drop (as is the case with other high humidity conditions, Figures 2b and 2d), and HNO<sub>2</sub> even shows a rising trend until 100% humidity. While the specific reasons for this are unclear at this point, we propose that the adverse effect of NH<sub>4</sub>NO<sub>x</sub> formation is still present, because otherwise the continuous rise of NH<sub>3</sub> concentrations should be observable. This question presents an important point for further research aimed at decreasing this loss mechanism, next to the use of an in-line HNO<sub>2</sub> removal.

However, as mentioned above, NH<sub>4</sub>NO<sub>2</sub> is not the only salt formed from NH<sub>3</sub> and HNO<sub>x</sub>. In our experiments, we observed the build-up of a fine white powder in the quartz tube used during the OES experiments. Qualitative analysis of the powder via the indophenol blue reaction (described elsewhere<sup>27,68</sup>) demonstrated that the cation of the salt was indeed NH<sub>4</sub><sup>+</sup>.<sup>24,47</sup> Due to the limited availability of analytical equipment, the anion could not be identified, but a negative Griess reagent test<sup>69</sup> excluded the presence of NO<sub>2</sub><sup>-</sup>. This is in agreement with NH<sub>4</sub>NO<sub>2</sub> not being a

stable product at atmospheric pressure and room temperature<sup>54</sup> (see Table 1). Therefore, we conclude that the anion was likely  $\text{NO}_3^-$ , in agreement with Zhu et al.<sup>44</sup>, who observed  $\text{NH}_4\text{NO}_3$  dust formation after operating plasma which contained both  $\text{NH}_3$  and  $\text{NO}_x$ . We note, however, that the amount of solid formed after weeks of our experiments (at different flow rates and humidity values) was in the range of mg. This is due to the (likely) very low amount of  $\text{HNO}_3$  formed in our plasma.<sup>70</sup> Indeed, although low concentrations of  $\text{HNO}_3$  would be expected in our experiments because substantial amounts of  $\text{NO}_2$  are produced in the gas phase with air plasma, no  $\text{HNO}_3$  was detected. Hence, it is reasonable to conclude that all formed  $\text{HNO}_3$  reacted with  $\text{NH}_3$  to form  $\text{NH}_4\text{NO}_3$ . Interestingly, when liquid  $\text{H}_2\text{O}$  was used to accumulate the NF products, both  $\text{NO}_3^-$  and  $\text{NH}_4^+$  were detected in PTW with air plasma. In case of a close liquid surface,  $\text{NH}_4\text{NO}_3$  did not precipitate out of the gas phase due to the short flight time to the liquid surface. Liquid water prevents decomposition via dissolution; the coordination of ions with water molecules in solution stabilizes the ions and inhibits decomposition reactions.

Furthermore, a semi-quantitative assessment of the relative loss pathways in this case was performed, with humid air. We performed the experiment with 2 L/min of air, 100% RH, for 3 h, during which we observed precipitate deposition on the tubing. After this, a gravimetric analysis of the precipitate was performed by washing the precipitate off the walls of the tubing. After evaporation of water, the mass of the accumulated precipitate was found to be below 5 mg. As shown above, by introducing the alkaline washer, 50 ppm of  $\text{NH}_3$  was “recovered” under these conditions (we note once again that the alkaline washer is not selective, and removes  $\text{HNO}_x$  rather than only  $\text{HNO}_2$  or only  $\text{HNO}_3$ ). This amounts to ca. 74 nmol/s of  $\text{NH}_3$ . From the stoichiometry of  $\text{NH}_4\text{NO}_3$  formation, we conclude that after 3 h the amount of precipitate would constitute 64 mg if all of it was  $\text{NH}_4\text{NO}_3$  – which is not the case. Thus, the relative contribution

of the  $\text{NH}_4\text{NO}_3$  pathway to  $\text{NH}_3$  loss does not exceed 10%. Therefore, even in the humid air plasma, most of  $\text{NH}_3$  is lost via the generation and subsequent decomposition of  $\text{NH}_4\text{NO}_2$ .

Although performance optimization is not the focus of this work, we also assessed the energy consumption (EC) and the production rate (PR) of NF in our experiments. The numerical EC values and the calculation method are presented in the supporting information in Table S5 and S6. The relative improvement in a hypothetical scenario when  $\text{NH}_3$  and  $\text{HNO}_2/\text{HNO}_3$  are not lost in our experiments was evaluated. Let us consider example conditions of humid air plasma operated at 2 L/min, 100% RH, i.e. the same conditions at which the experiment with the  $\text{HNO}_x$ -removing washer was performed. Here, we detect 50 ppm of  $\text{NH}_3$ , which means also 50 ppm  $\text{HNO}_x$  was lost. The overall concentration of NF products without accounting for the  $\text{NH}_4\text{NO}_x$  loss is ca. 300 ppm (see Figure 2d), which becomes 400 ppm when  $\text{NH}_4\text{NO}_x$  is not lost. Therefore, the relative decrease in EC, and the relative increase in PR, when the product loss is avoided amounts to ca. 30%. Using liquid water as a reservoir to accumulate the nitrogen fixation products can aid in this. Taken together, these data clearly suggest that using liquid  $\text{H}_2\text{O}$  in proximity to the plasma zone is beneficial: it increases the total net accumulation of the NF products, because it reduces or even eliminates the loss of  $\text{NH}_4\text{NO}_x$ .

## CONCLUSIONS

We studied the pathways of nitrogen fixation in humid  $\text{N}_2$  and humid air plasma using optical emission spectroscopy and Fourier-transform infrared spectroscopy. We revealed that the increased NH emission, as well as NH ground state density, strongly correlates with the water vapor content in both  $\text{N}_2$  and air plasmas, indicating that the reduction nitrogen fixation pathway (towards  $\text{NH}_3$  formation) takes place in both gas mixtures.

We show for the first time that  $\text{NH}_3$  is produced in air plasma in non-negligible quantities (in the same order of magnitude as  $\text{HNO}_2$ , and only an order of magnitude lower than  $\text{NO}$  and  $\text{NO}_2$  combined). However, in both air and  $\text{N}_2$ , this nitrogen fixation pathway is strongly affected by the presence of  $\text{HNO}_2$  and  $\text{HNO}_3$ .

In humid air, the formation of both  $\text{NH}_4\text{NO}_3$  and  $\text{NH}_4\text{NO}_2$  likely occurs. Although both of these can decrease the process efficiency downstream, part of  $\text{NH}_3$  remains in fixated form as precipitated  $\text{NH}_4\text{NO}_3$ . In contrast, in humid  $\text{N}_2$  we ascribe the loss pathway exclusively to  $\text{NH}_4\text{NO}_2$ , which is unstable and decomposes to  $\text{N}_2$  and  $\text{H}_2\text{O}$ , decreasing the overall nitrogen fixation efficiency.

In summary, our work shows that (1) the selectivity of nitrogen fixation in air and  $\text{N}_2$  plasmas can be controlled by changing the humidity of the feed gas, (2)  $\text{NH}_3$  production can be achieved in both  $\text{N}_2$  and air plasma using  $\text{H}_2\text{O}$  as a hydrogen source, and (3) the adverse effects of  $\text{NH}_4\text{NO}_2$  formation hinder the net production, and therefore the overall efficiency, of the plasma-based nitrogen fixation process. The latter means that, under conditions where  $\text{HNO}_2$  and  $\text{NH}_3$  are produced simultaneously, it is important to suppress the reverse process (via decomposition of  $\text{NH}_4\text{NO}_2$ ). This can be performed through an in-line removal of  $\text{HNO}_2$  from the gas mixture, or by using plasma-treated water to accumulate all nitrogen fixated products simultaneously without losses.

ASSOCIATED CONTENT

**Supporting Information**

The supporting information is available free of charge at <https://pubs.ac.org/...> (PDF), and includes additional details on the experimental setups of optical analyses, calculational methodology for OES and FTIR, and further experimental data.

## AUTHOR INFORMATION

### **Corresponding Author**

\*E-mail: [elise.vervloessem@uantwerpen.be](mailto:elise.vervloessem@uantwerpen.be).

### **Author Contributions**

The manuscript was written through contributions of all authors. All authors have given approval to the final version of the manuscript. \*These authors contributed equally.

### **Funding Sources**

This research is supported by the Excellence of Science FWO-FNRS project (NITROPLASM, FWO grant ID GoF9618n, EOS ID 30505023), the European Research Council (ERC) under the European Union's Horizon 2020 research and innovation programme (grant №810182 – SCOPE ERC Synergy project), and the Fund for Scientific Research (FWO) Flanders Bio-economy project (grant № G0G2322N), funded by the European Union -NextGenerationEU.

## ACKNOWLEDGMENT

We would like to thank E. H. Choi and coworkers from the Plasma Bioscience Research Center (Republic of Korea) for providing the plasma jet used in this work.

## ABBREVIATIONS

HB, Haber-Bosch process; NF, nitrogen fixation; PTW, plasma-treated water; UV, ultra violet; EC, energy consumption; FTIR, Fourier transform infrared spectroscopy; OES, optical emission spectroscopy; MFC, mass flow controller; Ls, standard liter.

## REFERENCES

- (1) Smil, V. Nitrogen and Food Production: Proteins for Human Diets. *Ambio* **2002**, *31* (2), 126–131. <https://doi.org/10.1579/0044-7447-31.2.126>.
- (2) Appl, M. Ammonia, 2. Production Processes. In *Ullmann's Encyclopedia of Industrial Chemistry*; Wiley-VCH Verlag GmbH & Co. KGaA, 2011. [https://doi.org/10.1002/14356007.o02\\_o11](https://doi.org/10.1002/14356007.o02_o11).
- (3) Erisman, J. W.; Sutton, M. a; Galloway, J.; Klimont, Z.; Winiwarter, W. How a Century of Ammonia Synthesis Changed the World. *Nat. GeoSci.* **2008**, *1* (October 2008), 636–639. <https://doi.org/10.1038/ngeo325>.
- (4) Nayak-luke, R. M.; Banares-Alcantare, R. Techno-Economic Viability of Islanded Green Ammonia as a Carbon-Free Energy Vector and as a Substitute for Conventional Production. *Energy Environ. Sci.* **2020**, *13*, 2957–2966. <https://doi.org/10.1039/D0EE01707H>.
- (5) Bicer, Y.; Dincer, I.; Zamfirescu, C.; Vezina, G.; Raso, F. Comparative Life Cycle Assessment of Various Ammonia Production Methods. *J. Clean. Prod.* **2016**, *135*, 1379–1395. <https://doi.org/10.1016/J.JCLEPRO.2016.07.023>.
- (6) Cherkasov, N.; Ibhaddon, A. O.; Fitzpatrick, P. A Review of the Existing and Alternative Methods for Greener Nitrogen Fixation. *Chem. Eng. Process.* **2015**, *90*, 24–33. <https://doi.org/10.1016/j.cep.2015.02.004>.
- (7) Anastasopoulou, A.; Butala, S.; Lang, J.; Hessel, V.; Wang, Q. Life Cycle Assessment of the Nitrogen Fixation Process Assisted by Plasma Technology and Incorporating Renewable Energy. *Ind. Eng. Chem. Res.* **2016**, *55*, 8141–8153. <https://doi.org/10.1021/acs.iecr.6b00145>.
- (8) Hochman, G.; Goldman, A. S.; Felder, F. A.; Mayer, J. M.; Miller, A. J. M.; Holland, P. L.; Goldman, L. A.; Manocha, P.; Song, Z.; Aleti, S. Potential Economic Feasibility of Direct Electrochemical Nitrogen Reduction as a Route to Ammonia. *ACS Sust. Chem. Eng.* **2020**, *8* (24), 8938–8948. <https://doi.org/10.1021/acssuschemeng.0c01206>.

- (9) Bogaerts, A.; Neyts, E. C. Plasma Technology: An Emerging Technology for Energy Storage. *ACS Energy Lett.* **2018**, *3* (4), 1013–1027. <https://doi.org/10.1021/acsenerylett.8b00184>.
- (10) Winter, L. R.; Chen, J. G. N<sub>2</sub> Fixation by Plasma-Activated Processes. *Joule* **2021**, *5* (2), 300–315. <https://doi.org/10.1016/J.JOULE.2020.11.009>.
- (11) Patil, B. S.; Wang, Q.; Hessel, V.; Lang, J. Plasma N<sub>2</sub> -Fixation : 1900 – 2014. *Catal* **2015**, *256*, 49–66. <https://doi.org/10.1016/j.cattod.2015.05.005>.
- (12) Vervloessem, E.; Aghaei, M.; Jardali, F.; Hafezkhiani, N.; Bogaerts, A. Plasma-Based N<sub>2</sub> Fixation into NO<sub>x</sub>: Insights from Modeling toward Optimum Yields and Energy Costs in a Gliding Arc Plasmatron. *ACS Sustain. Chem. Eng.* **2020**, *8* (26), 9711–9720. <https://doi.org/10.1021/acssuschemeng.0c01815>.
- (13) Jardali, F.; van Alphen, S.; Creel, J.; Ahmadi Eshtehardi, H.; Axelsson, M.; Ingels, R.; Snyders, R.; Bogaerts, A. NO<sub>x</sub> Production in a Rotating Gliding Arc Plasma: Potential Avenue for Sustainable Nitrogen Fixation . *Green Chem.* **2021**, *23*, 1748–1757. <https://doi.org/10.1039/d0gc03521a>.
- (14) Kelly, S.; Bogaerts, A. Nitrogen Fixation in an Electrode-Free Microwave Plasma. *Joule* **2021**, *5* (11), 3006–3030. <https://doi.org/10.1016/j.joule.2021.09.009>.
- (15) van Alphen, S.; Ahmadi Eshtehardi, H.; O’Modhain, C.; Bogaerts, J.; van Poyer, H.; Creel, J.; Delplancke, M. P.; Snyders, R.; Bogaerts, A. Effusion Nozzle for Energy-Efficient NO<sub>x</sub> Production in a Rotating Gliding Arc Plasma Reactor. *Chem. Eng. J.* **2022**, *443*, 136529–136541. <https://doi.org/10.1016/J.CEJ.2022.136529>.
- (16) Rouwenhorst, K. H. R.; Engelmann, Y.; van ’T Veer, K.; Postma, R. S.; Bogaerts, A.; Lefferts, L. Plasma-Driven Catalysis: Green Ammonia Synthesis with Intermittent Electricity. *Green Chem.* **2020**, *22* (19), 6258–6287. <https://doi.org/10.1039/d0gc02058c>.
- (17) Carreon, M. L. Plasma Catalytic Ammonia Synthesis : State of the Art and Future Directions. *J. Phys. D: Appl. Phys.* **2019**, *52*, 483001–483025. <https://doi.org/10.1088/1361-6463/ab3b2c>.
- (18) Huang, Z.; Xiao, A.; Liu, D.; Lu, X.; Ostrikov, K. Plasma-Water-Based Nitrogen Fixation: Status, Mechanisms, and Opportunities. *Plasma Processes Polym.* **2022**, *19* (4), 2100198–2100211. <https://doi.org/10.1002/PPAP.202100198>.
- (19) Chehade, G.; Dincer, I. Progress in Green Ammonia Production as Potential Carbon-Free Fuel. *Fuel* **2021**, *299*, 120845–120879. <https://doi.org/10.1016/J.FUEL.2021.120845>.
- (20) Peng, P.; Chen, P.; Addy, M.; Cheng, Y.; Zhang, Y.; Anderson, E.; Zhou, N.; Schiappacasse, C.; Hatzenbeller, R. In Situ Plasma-Assisted Atmospheric Nitrogen Fixation Using Water and Spray-Type Jet Plasma†. *Chem. Commun.* **2018**, *54*, 2886–2889. <https://doi.org/10.1039/C8CC00697K>.



- (21) Peng, P.; Schiappacasse, C.; Zhou, N.; Addy, M.; Cheng, Y.; Zhang, Y.; Anderson, E.; Chen, D.; Wang, Y.; Liu, Y.; Chen, P.; Ruan, R. Plasma in Situ Gas-Liquid Nitrogen Fixation Using Concentrated High-Intensity Electric Field. *J. Phys. D: Appl. Phys.* **2019**, *52* (49), 494001–494009. <https://doi.org/10.1088/1361-6463/ab3ea6>.
- (22) Kumari, S.; Pishgar, S.; Schwarting, M. E.; Paxton, W. F.; Spurgeon, J. M. Synergistic Plasma-Assisted Electrochemical Reduction of Nitrogen to Ammonia. *Chem. Commun.* **2018**, *54* (95), 13347–13350. <https://doi.org/10.1039/c8cc07869f>.
- (23) Sakakura, T.; Takatsuji, Y.; Morimoto, M.; Haruyama, T. Nitrogen Fixation through the Plasma/Liquid Interfacial Reaction with Controlled Conditions of Each Phase as the Reaction Locus. *Electrochemistry* **2020**, *88* (3), 190–194. <https://doi.org/10.5796/electrochemistry.19-00080>.
- (24) Sakakura, T.; Murakami, N.; Takatsuji, Y.; Haruyama, T. Nitrogen Fixation in a Plasma/Liquid Interfacial Reaction and Its Switching between Reduction and Oxidation. *J. Phys. Chem. C* **2020**, *124* (17), 9401–9408. <https://doi.org/10.1021/acs.jpcc.0c02392>.
- (25) Sakakura, T.; Murakami, N.; Takatsuji, Y.; Morimoto, M.; Haruyama, T. Contribution of Discharge Excited Atomic N, N<sub>2</sub><sup>\*</sup>, and N<sub>2</sub><sup>+</sup> to a Plasma/Liquid Interfacial Reaction as Suggested by Quantitative Analysis. *ChemPhysChem* **2019**, *20* (11), 1467–1474. <https://doi.org/10.1002/cphc.201900212>.
- (26) Sakakura, T.; Uemura, S.; Hino, M.; Kiyomatsu, S.; Takatsuji, Y.; Yamasaki, R.; Morimoto, M.; Haruyama, T. Excitation of H<sub>2</sub>O at the Plasma/Water Interface by UV Irradiation for the Elevation of Ammonia Production. *Green Chem.* **2018**, *20* (3), 627–633. <https://doi.org/10.1039/c7gc03007j>.
- (27) Haruyama, T.; Namise, T.; Shimoshimizu, N.; Uemura, S.; Takatsuji, Y.; Hino, M.; Yamasaki, R.; Kamachi, T.; Kohno, M. Non-Catalyzed One-Step Synthesis of Ammonia from Atmospheric Air and Water. *Green Chem.* **2016**, *18* (16), 4536–4541. <https://doi.org/10.1039/c6gc01560c>.
- (28) Sun, J.; Alam, D.; Daiyan, R.; Masood, H.; Zhang, T.; Zhou, R.; Cullen, P. J.; Lovell, E. C.; Jalili, A. (Rouhollah); Amal, R. A Hybrid Plasma Electrocatalytic Process for Sustainable Ammonia Production. *Energy Environ. Sci.* **2021**, *14*, 865–872. <https://doi.org/10.1039/d0ee03769a>.
- (29) Hawtof, R.; Ghosh, S.; Guarr, E.; Xu, C.; Sankaran, R. M.; Renner, J. N. Catalyst-Free, Highly Selective Synthesis of Ammonia from Nitrogen and Water by a Plasma Electrolytic System. *Sci. Adv.* **2019**, *5* (1), eaat5778-9. <https://doi.org/10.1126/sciadv.aat5778>.
- (30) Sharma, R. K.; Patel, H.; Mushtaq, U.; Kyriakou, V.; Zafeiropoulos, G.; Peeters, F.; Welzel, S.; van de Sanden, M. C. M.; Tsampas, M. N. Plasma Activated Electrochemical Ammonia Synthesis from Nitrogen and Water. *ACS Energy Lett.* **2021**, *6* (2), 313–319. <https://doi.org/10.1021/acsenenergylett.0c02349>.

- (31) Chen, H.; Yuan, D.; Wu, A.; Lin, X.; Li, X. Review of Low-Temperature Plasma Nitrogen Fixation Technology. *Waste Disposal and Sustainable Energy*. Springer September 1, 2021, pp 201–217. <https://doi.org/10.1007/s42768-021-00074-z>.
- (32) Gorbanev, Y.; Vervloessem, E.; Nikiforov, A.; Bogaerts, A. Nitrogen Fixation with Water Vapor by Nonequilibrium Plasma: Toward Sustainable Ammonia Production. *ACS Sust. Chem. Eng.* **2020**, *8*, 2996–3004. <https://doi.org/10.1021/acssuschemeng.9b07849>.
- (33) Zhang, T.; Zhou, R.; Zhang, S.; Zhou, R.; Ding, J.; Li, F.; Hong, J.; Dou, L.; Shao, T.; Murphy, A. B.; Ostrikov, K.; Cullen, P. J. Sustainable Ammonia Synthesis from Nitrogen and Water by One-Step Plasma Catalysis. *Energy Environ. Mater.* **2022**. <https://doi.org/10.1002/eem2.12344>.
- (34) Rouwenhorst, K. H. R.; Jardali, F.; Bogaerts, A.; Lefferts, L. From the Birkeland-Eyde Process towards Energy-Efficient Plasma- Based NOX Synthesis: A Techno-Economic Analysis. *Energy Environ. Sci.* **2021**, *14*, 2520–2534. <https://doi.org/https://doi.org/10.1039/D0EE03763J>.
- (35) Vervloessem, E.; Gorbanev, Y.; Nikiforov, A.; de Geyter, N.; Bogaerts, A. Sustainable NOx Production from Air in Pulsed Plasma: Elucidating the Chemistry behind the Low Energy Consumption. *Green Chem.* **2022**, *24*, 916–929. <https://doi.org/10.1039/d1gc02762j>.
- (36) Hollevoet, L.; Vervloessem, E.; Gorbanev, Y.; Nikiforov, A.; de Geyter, N.; Bogaerts, A.; Martens, J. A. Energy-Efficient Small-Scale Ammonia Synthesis Process with Plasma-Enabled Nitrogen Oxidation and Catalytic Reduction of Adsorbed NOx. *ChemSusChem* **2022**, *15* (10), e202102526. <https://doi.org/10.1002/cssc.202102526>.
- (37) Toth, J. R.; Abuyazid, N. H.; Lacks, D. J.; Renner, J. N.; Sankaran, R. M. A Plasma-Water Droplet Reactor for Process-Intensified, Continuous Nitrogen Fixation at Atmospheric Pressure. *ACS Sust. Chem. Eng.* **2020**, *8* (39), 14845–14854. <https://doi.org/10.1021/acssuschemeng.0c04432>.
- (38) Gorbanev, Y.; Verlackt, C. C. W.; Tinck, S.; Tuenter, E.; Foubert, K.; Cos, P.; Bogaerts, A. Combining Experimental and Modelling Approaches to Study the Sources of Reactive Species Induced in Water by the COST RF Plasma Jet. *Phys. Chem. Chem. Phys.* **2018**, *20* (4), 2797–2808. <https://doi.org/10.1039/c7cp07616a>.
- (39) Gorbanev, Y.; O’Connell, D.; Chechik, V. Non-Thermal Plasma in Contact with Water: The Origin of Species. *Chem. Eur. J.* **2016**, *22* (10), 3496–3505. <https://doi.org/10.1002/chem.201503771>.
- (40) Gordon, I.E., Rothman, L.S., Hargreaves, R.J., Hashemi, R., Karlovets, E.V., Skinner, F.M., Conway, E.K., Hill, C., Kochanov, R.V., Tan, Y., Wcisło, P., Finenko, A.A., Nelson, K., Bernath, P.F., Birk, M., Boudon, V., Campargue, A., Chance, K.V., Coustenis, S. N. The HITRAN2020 Molecular Spectroscopic Database. *J. Quant. Spectrosc. Radiat. Transf.* **2022**, *277*, 107949.

- (41) Barney, W. S.; Wingen, L. M.; Lakin, M. J.; Brauers, T.; Stutz, J.; Finlayson-Pitts, B. J. Infrared Absorption Cross-Section Measurements for Nitrous Acid (HONO) at Room Temperature. *J. Phys. Chem. A* **2000**, *104* (8), 1692–1699. <https://doi.org/10.1021/jp9930503>.
- (42) Pearse, R. W. B.; Gaydon, A. G. *Identification of Molecular Spectra*; Chapman & Hall LTD: London, 1950; Vol. Second Edition.
- (43) Lieberman, M. A.; Lichtenberg, A. J. *Principles of Plasma Discharges and Plasma Materials Processing*, second.; John Wiley & Sons: New Jersey, 2005.
- (44) Zhu, Y.; Xiong, Z.; Li, M.; Chen, X.; Lu, C. Investigation of NH<sub>4</sub>NO<sub>3</sub> Formation by Air Plasma and Wasted Ammonia. *Plasma Process Polym.* **2021**, *18* (8), 1–7. <https://doi.org/10.1002/ppap.202000223>.
- (45) Bruggeman, P.; Brandenburg, R. Atmospheric Pressure Discharge Filaments and Microplasmas: Physics, Chemistry and Diagnostics. *J. Phys. D: Appl. Phys.* **2013**, *46* (46), 464001–464029. <https://doi.org/10.1088/0022-3727/46/46/464001>.
- (46) van Duc Long, N.; Al-Bared, M.; Lin, L.; Davey, K.; Tran, N. N.; Pourali, N.; Ken Ostrikov, K.; Rebrov, E.; Hessel, V. Understanding Plasma-Assisted Ammonia Synthesis via Crossing Discipline Borders of Literature: A Critical Review. *Chem. Eng. Sci.* **2022**, *263*, 118097–118110. <https://doi.org/10.1016/J.CES.2022.118097>.
- (47) Liu, Y.; Tan, Z.; Chen, X.; Li, X.; Wang, X. A Numerical Investigation on the Effects of Water Vapor on Electron Energy and Oh Production in Atmospheric-Pressure He/H<sub>2</sub>O and Ar/H<sub>2</sub>O Plasma Jets. *IEEE Trans Plasma Sci.* **2019**, *47* (3), 1593–1604. <https://doi.org/10.1109/TPS.2019.2896060>.
- (48) Mo, Y.; Ottinger, C.; Shen, G. Collision-Induced Intersystem Crossing from NH(A1Δ, b 1Σ<sup>+</sup>) to NH(A3Π): Gateway-Mediated and Direct Mechanisms. *J. Chem. Phys.* **1999**, *111* (10), 4598–4612. <https://doi.org/10.1063/1.479221>.
- (49) Buckley, S. G.; Damm, C. J.; Vitovec, W. M.; Anne Sgro, L.; Sawyer, R. F.; Koshland, C. P.; Lucas, D. Ammonia Detection and monitoring with Photofragmentation Fluorescence. *Appl. Opt.* **1998**, *37*, 8382–8391. <https://doi.org/https://doi.org/10.1364/AO.37.008382>.
- (50) Hofzumahaus, A.; Stuhl, F. Electronic Quenching, Rotational Relaxation, and Radiative Lifetime of NH(A3Π, V'=0, N'). *J. Chem. Phys.* **1984**, *82* (7), 3152–3159. <https://doi.org/10.1063/1.448213>.
- (51) Jiang, B.; Zhao, S.; Wang, Y.; Wenren, Y.; Zhu, Z.; Harding, J.; Zhang, X.; Tu, X.; Zhang, X. Plasma-Enhanced Low Temperature NH<sub>3</sub>-SCR of NO<sub>x</sub> over a Cu-Mn/SAPO-34 Catalyst under Oxygen-Rich Conditions. *Appl. Catal. B* **2021**, *286*, 119886–119897. <https://doi.org/10.1016/j.apcatb.2021.119886>.
- (52) Grossale, A.; Nova, I.; Tronconi, E.; Chatterjee, D.; Weibel, M. The Chemistry of the NO/NO<sub>2</sub>-NH<sub>3</sub> “Fast” SCR Reaction over Fe-ZSM5 Investigated by Transient

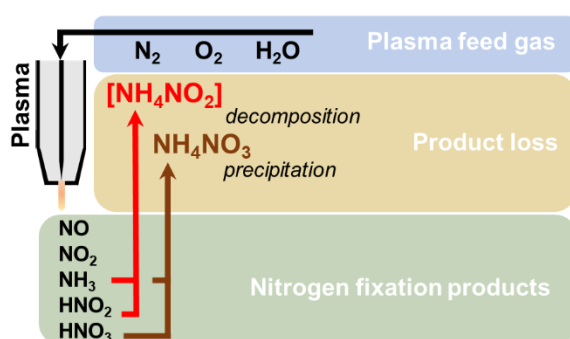
- Reaction Analysis. *J. Catal.* **2008**, *256* (2), 312–322. <https://doi.org/10.1016/j.jcat.2008.03.027>.
- (53) Kubota, H.; Liu, C.; Toyao, T.; Maeno, Z.; Ogura, M.; Nakazawa, N.; Inagaki, S.; Kubota, Y.; Shimizu, K.-I. Formation and Reactions of NH<sub>4</sub>NO<sub>3</sub> during Transient and Steady-State NH<sub>3</sub>-SCR of NO<sub>x</sub> over H-AFX Zeolites: Spectroscopic and Theoretical Studies. *ACS Catal.* **2020**, *10* (3), 2334–2344. <https://doi.org/https://doi.org/10.1021/acscatal.9b05151>.
- (54) Mebel, A. M.; Lh, M. C.; Morokuma, K.; Melius, C. F. Theoretical Study of the Gas-Phase Structure, Thermochemistry, and Decomposition Mechanisms of NH<sub>4</sub>NO<sub>2</sub> and NH<sub>4</sub>(NO<sub>2</sub>)<sub>2</sub>. *J. Phys. Chem.* **1995**, *99* (18), 6842–6848. <https://doi.org/https://doi.org/10.1021/j100018a015>.
- (55) Sun, Q.; Gao, Z.-X.; Wen, B.; Sachtler, W. M. H. Spectroscopic Evidence for a Nitrite Intermediate in the Catalytic Reduction of NO<sub>x</sub> with Ammonia on Fe/MFI. *Catal. Letters* **2002**, *78*, 1–5. <https://doi.org/https://doi.org/10.1023/A:1014981206924>.
- (56) Savara, A.; Li, M. J.; Sachtler, W. M. H.; Weitz, E. Catalytic Reduction of NH<sub>4</sub>NO<sub>3</sub> by NO: Effects of Solid Acids and Implications for Low Temperature DeNO<sub>x</sub> Processes. *Appl. Catal. B* **2008**, *81* (3–4), 251–257. <https://doi.org/10.1016/j.apcatb.2007.12.008>.
- (57) Zhang, X.; Zhang, Y.; Lu, H.; Zhu, Z.; Han, J. Characteristics of Ammonia Oxidation in a Dielectric Barrier Discharge Reactor. *IEEE Trans. Plasma Sci.* **2020**, *48* (10), 3616–3620. <https://doi.org/10.1109/TPS.2020.3025092>.
- (58) Kim, D.-J.; Choi, Y.; Kim, K.-S. Effects of Process Variables on NO<sub>x</sub> Conversion by Pulsed Corona Discharge Process. *Plasma Chem. Plasma Process.* **2001**, *21* (4), 625–650. <https://doi.org/https://doi.org/10.1023/A:1012007319848>.
- (59) Atkinson, R.; Baulch, D. L.; Cox, R. A.; Crowley, J. N.; Hampson, R. F.; Hynes, R. G.; Jenkin, M. E.; Rossi, M. J.; Troe, J.; Center, P. R.; Science, L. H.; Centre, T.; Park, S. Evaluated Kinetic and Photochemical Data for Atmospheric Chemistry: Volume I – Gas Phase Reactions of Ox, HO<sub>x</sub>, NO<sub>x</sub> and SO<sub>x</sub> Species. *J. Phys. Chem. Ref. Data* **2004**, *1*, 1461–1738. <https://doi.org/10.5194/acp-4-1461-2004>.
- (60) Hippler, H.; Krasteva, N.; Nasterlack, S.; Striebel, F. Reaction of OH + NO<sub>2</sub>: High Pressure Experiments and Falloff Analysis †. *J. Phys. Chem. A* **2006**, *110*, 6781–6788. <https://doi.org/10.1021/jp0562734>.
- (61) Pagsberg, P.; Ratajczak, E.; Sillesen, A.; Latajka, Z. Kinetics and Thermochemistry of the Reversible Gas Phase Reaction HONO + NH<sub>3</sub> = H<sub>3</sub>N-HONO Studied by Infrared Diode Laser Spectroscopy. *Chem. Phys. Lett.* **1994**, *227*, 6–12. [https://doi.org/https://doi.org/10.1016/0009-2614\(94\)00787-X](https://doi.org/https://doi.org/10.1016/0009-2614(94)00787-X).

- (62) Mozurkewich, M. The Dissociation Constant of Ammonium Nitrate and Its Dependence on Temperature, Relative Humidity and Particle Size. *Atmos Environ* **1993**, *27* (2), 261–270.
- (63) Vyazovkin, S.; Clawson, J. S.; Wight, C. A. Thermal Dissociation Kinetics of Solid and Liquid Ammonium Nitrate. *Chem. Mater.* **2001**, *13* (3), 960–966. <https://doi.org/10.1021/cm000708c>.
- (64) Shan, Y.; Shi, X.; He, G.; Liu, K.; Yan, Z.; Yu, Y.; He, H. Effects of NO<sub>2</sub> Addition on the NH<sub>3</sub>-SCR over Small-Pore Cu–SSZ-13 Zeolites with Varying Cu Loadings. *J. Phys. Chem. C* **2018**, *122* (45), 25948–25953. <https://doi.org/10.1021/acs.jpcc.8b05930>.
- (65) Feick, G.; Hainer, R. M. On the Thermal Decomposition of Ammonium Nitrate. Steady-State Reaction Temperatures and Reaction Rate. *J. Am. Chem. Soc.* **1954**, *76*, 5860–5863. <https://doi.org/https://doi.org/10.1021/ja01651a096>.
- (66) Li, M.; Henao, J.; Yeom, Y.; Weitz, E.; Sachtler, W. M. H. Low Activation Energy Pathway for the Catalyzed Reduction of Nitrogen Oxides to N<sub>2</sub> by Ammonia. *Catal. Letters* **2004**, *98*, 5–9. <https://doi.org/https://doi.org/10.1007/s10562-004-6441-y>.
- (67) Gordon, I. E.; Rothman, L. S.; Hargreaves, R. J.; Hashemi, R.; Karlovets, E. v.; Skinner, F. M.; Conway, E. K.; Hill, C.; Kochanov, R. v.; Tan, Y.; Weisło, P.; Finenko, A. A.; Nelson, K.; Bernath, P. F.; Birk, M.; Boudon, V.; Campargue, A.; Chance, K. v.; Coustenis, A.; Drouin, B. J.; Flaud, J. M.; Gamache, R. R.; Hodges, J. T.; Jacquemart, D.; Mlawer, E. J.; Nikitin, A. v.; Perevalov, V. I.; Rotger, M.; Tennyson, J.; Toon, G. C.; Tran, H.; Tyuterev, V. G.; Adkins, E. M.; Baker, A.; Barbe, A.; Canè, E.; Császár, A. G.; Dudaryonok, A.; Egorov, O.; Fleisher, A. J.; Fleurbaey, H.; Foltynowicz, A.; Furtenbacher, T.; Harrison, J. J.; Hartmann, J. M.; Horneman, V. M.; Huang, X.; Karman, T.; Karns, J.; Kassi, S.; Kleiner, I.; Kofman, V.; Kwabia-Tchana, F.; Lavrentieva, N. N.; Lee, T. J.; Long, D. A.; Lukashetskaya, A. A.; Lyulin, O. M.; Makhnev, V. Y.; Matt, W.; Massie, S. T.; Melosso, M.; Mikhailenko, S. N.; Mondelain, D.; Müller, H. S. P.; Naumenko, O. v.; Perrin, A.; Polyansky, O. L.; Raddaoui, E.; Raston, P. L.; Reed, Z. D.; Rey, M.; Richard, C.; Tóbiás, R.; Sadiek, I.; Schwenke, D. W.; Starikova, E.; Sung, K.; Tamassia, F.; Tashkun, S. A.; vander Auwera, J.; Vasilenko, I. A.; Viganin, A. A.; Villanueva, G. L.; Vispoel, B.; Wagner, G.; Yachmenev, A.; Yurchenko, S. N. The HITRAN2020 Molecular Spectroscopic Database. *J. Quant. Spectrosc. Radiat. Transf.* **2022**, *277*, 107949. <https://doi.org/10.1016/J.JQSRT.2021.107949>.
- (68) Bolleter W. T.; Bushman C. J.; Tiddwell P. W. Spectrophotometric Determination of Ammonia as Indophenol. *Anal. Chem.* **1961**, *33* (4), 592–594. <https://doi.org/https://doi.org/10.1021/ac60172a034>.
- (69) Hu, X.; Zhang, Y.; Antonio Wu, R.; Liao, X.; Liu, D.; Cullen, P. J.; Zhou, R.-W.; Ding, T. Diagnostic Analysis of Reactive Species in Plasma-Activated Water

(PAW): Current Advances and Outlooks. *J. Phys. D: Appl. Phys.* **2022**, *55*, 023002–023018. <https://doi.org/10.1088/1361-6463/ac286a>.

- (70) Janda, M.; Hensel, K.; Tóth, P.; Hassan, M. E.; Machala, Z.; Nastuta, V. The Role of HNO<sub>2</sub> in the Generation of Plasma-Activated Water by Air Transient Spark Discharge. *Appl. Sci.* **2021**, *11* (15), 7053–7073. <https://doi.org/10.3390/app11157053>.

### For Table of Contents Use Only



**SYNOPSIS** We demonstrate in-situ production of  $NH_3$  in nitrogen fixation from  $N_2$  and air with  $H_2O$  vapor, and show that the efficiency of the process can be increased by avoiding the consequent loss of  $NH_3$  via formation of  $NH_4NO_2$ .

# Supporting Information

## NH<sub>3</sub> and HNO<sub>x</sub> Formation and Loss in Nitrogen Fixation from Air with Water Vapor by Nonequilibrium Plasma

*Elise Vervloessem<sup>†,‡,\*</sup>, Mikhail Gromov<sup>‡,†</sup>, Nathalie De Geyter<sup>‡</sup>, Annemie Bogaerts<sup>†</sup>, Yury*

*Gorbanev<sup>†,x</sup>, Anton Nikiforov<sup>‡,x</sup>*

<sup>†</sup>Research group PLASMANT, Department of Chemistry, University of Antwerp,

Universiteitsplein 1, 2610 Wilrijk, Belgium

<sup>‡</sup>Research Unit Plasma Technology (RUPT), Department of Applied Physics, Ghent

University, Sint-Pietersnieuwstraat 41, 9000 Ghent, Belgium

<sup>†</sup>Chimie des Interactions Plasma Surface (ChiPS), CIRMAP, Mons University, 20 Place du

Parc, 7000 Mons, Belgium

\*[elise.vervloessem@uantwerpen.be](mailto:elise.vervloessem@uantwerpen.be)

**Pages: 24**

**Figures: 5**

**Tables: 6**

## Contents

<i>S1. Schematic of the plasma device</i> .....	s3
<b>Figure S1.</b> Various pathways for plasma-based nitrogen fixation with a focus on the different possible hydrogen sources. The current industrial process is shown as a reference in blue. Each full line represents a possible pathway towards basic fertilizer chemicals.....	s3
<i>S2. Schematic of the plasma device</i> .....	s3
<b>Figure S2.</b> Schematic of the plasma device. HV stands for high voltage electrode. ....	s3
<i>S3. FTIR analysis</i> .....	s4
<b>Figure S3.</b> (a) Overview of absorption bands from NO, NO <sub>2</sub> , N <sub>2</sub> O, HNO <sub>3</sub> , HNO <sub>2</sub> , NH <sub>3</sub> and O <sub>3</sub> . (b) HNO <sub>2</sub> and HNO <sub>3</sub> bands in the 3400 – 3800 cm <sup>-1</sup> region. (c) HNO <sub>2</sub> , HNO <sub>3</sub> , NO and NO <sub>2</sub> bands in the 1550 – 1850 cm <sup>-1</sup> region. (d) HNO <sub>2</sub> and HNO <sub>3</sub> bands in the 1100 - 1500 cm <sup>-1</sup> region. (e) HNO <sub>2</sub> and HNO <sub>3</sub> bands in the 700 - 1100 cm <sup>-1</sup> region. All simulated spectra have been taken from the HITRAN database <sup>1</sup> , except for HNO <sub>2</sub> and the HNO <sub>3</sub> region 3700 – 3800 cm <sup>-1</sup> annotated with dashed lines, which were digitized from Pipa et al. <sup>6</sup> based on literature values. <sup>7,8</sup> .....	s5
<i>S4. Experimental setups of OES</i> .....	s5
<b>Figure S4.</b> Basic gas analysis experimental setup as explained in the main text. (a) OES setup axial to the jet. (b) OES setup perpendicular to the afterglow using 10 fibers for spatially resolved measurements (1-10 mm from the nozzle). ....	s5
<i>S5. Optical emission spectroscopy</i> .....	s5
S5.1. Correction for quenching by H <sub>2</sub> O, O <sub>2</sub> and N <sub>2</sub> .....	s6
<b>Table S1.</b> Einstein transitions coefficients of NH(A <sup>3</sup> Π-X <sup>3</sup> Σ) and NO(A <sup>2</sup> Σ <sup>+</sup> ).....	s7
<b>Table S2.</b> The cross sections and rate coefficients for NH(A <sup>3</sup> Π) and NO(A <sup>2</sup> Σ <sup>+</sup> ) quenching by N <sub>2</sub> , O <sub>2</sub> and H <sub>2</sub> O as collisional quenchers.....	s7
S5.2 Correction for sensitivity .....	s7
S5.3 Correction for excitation probability.....	s7
<i>S6. NO<sub>x</sub> formation in (humid) N<sub>2</sub> and air</i> .....	s8
<b>Table S3.</b> (Extended) Zeldovich reactions, their corresponding reaction rate coefficients and relevant temperature ranges. ....	s9
<i>S7. OES spectra recorded perpendicular to the plasma effluent</i> .....	s9
<b>Table S4.</b> Overview of the waterfall plot conditions and their respective Figure numbers. ....	s9
<b>Figure S5.</b> Emission spectra (334–340 nm) as a function of the distance from the jet nozzle (1–10 mm). The full list of the experimental conditions (Figures S5a – S5t) is shown in Table S3 above.....	s10
<i>S8. Energy consumption and production rate</i> .....	s20



**Table S5.** Average energy consumption (EC) of nitrogen fixation. ....s21

**Table S6.** Average production rate (PR) of the products of nitrogen fixation, and the conversion of  $N_2$ . ....s22

*S1. Schematic of the plasma device*

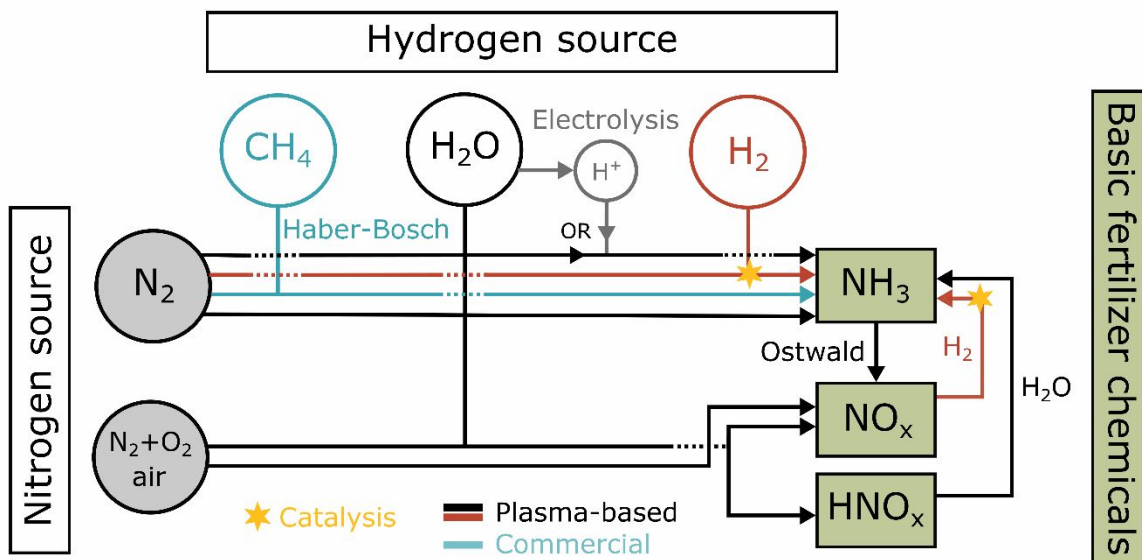


**Figure S1.** Various pathways for plasma-based nitrogen fixation with a focus on the different possible hydrogen sources. The current industrial process is shown as a reference in blue. Each full line represents a possible pathway towards basic fertilizer chemicals.

*S2. Schematic of the plasma device*

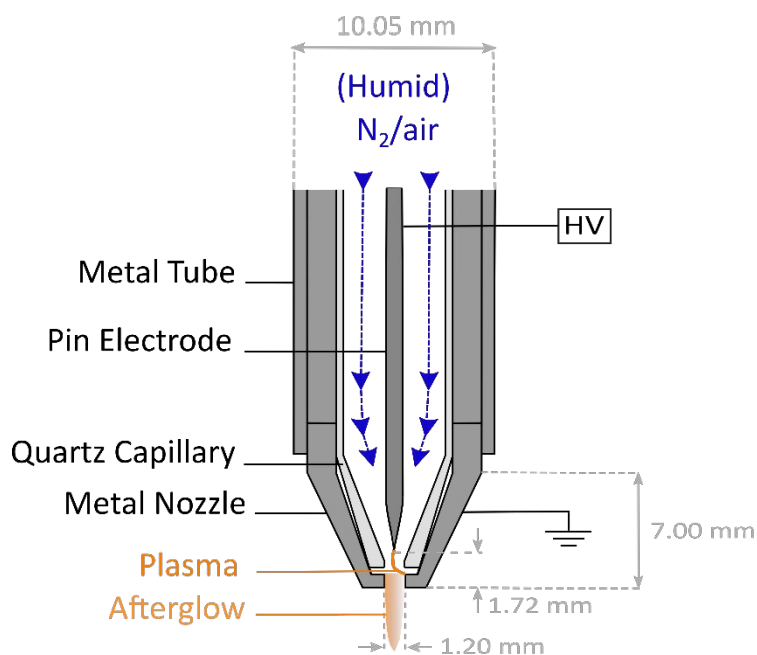


**Figure S2.** Schematic of the plasma device. HV stands for high voltage electrode.

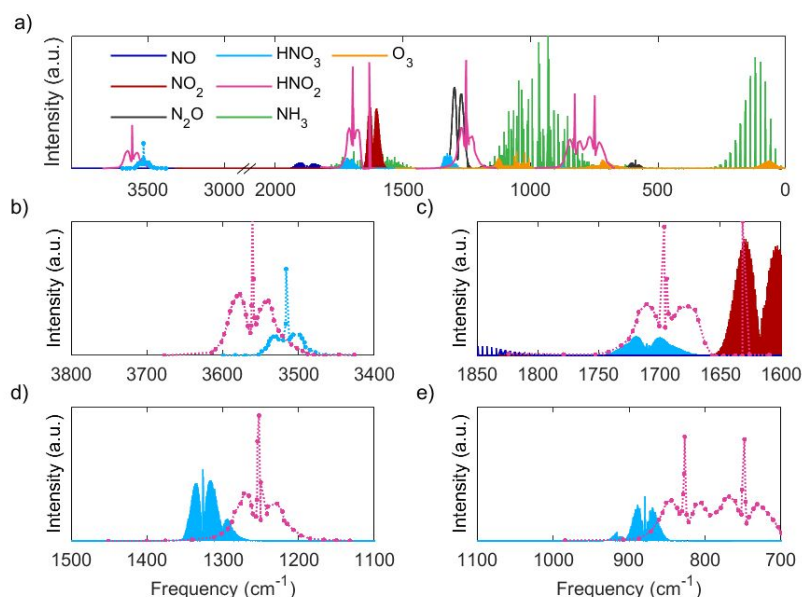
### S3. FTIR analysis

Absorbance spectra measured by Fourier transform infrared spectroscopy revealed the presence of several vibrational transitions which correspond to NO, NO<sub>2</sub>, N<sub>2</sub>O, NH<sub>3</sub>, and HNO<sub>2</sub> species. The Bruker system (with the OPUS gas analysis software) was factory-calibrated for NO, NO<sub>2</sub>, N<sub>2</sub>O, O<sub>3</sub> and N<sub>2</sub>O<sub>5</sub>. The remaining peaks were identified using the HITRAN database.<sup>1</sup> Their concentrations were determined by measuring a reference signal from the gas mixture with a known concentration of the species of interest and *via* Beer's law as follows<sup>2</sup>:

$$n_j = \frac{\ln(I^{(v)}/I_0^{(v)})}{\sigma_j(v) \cdot L} \times \left(\frac{10^{12}}{n}\right) \quad (\text{S1})$$

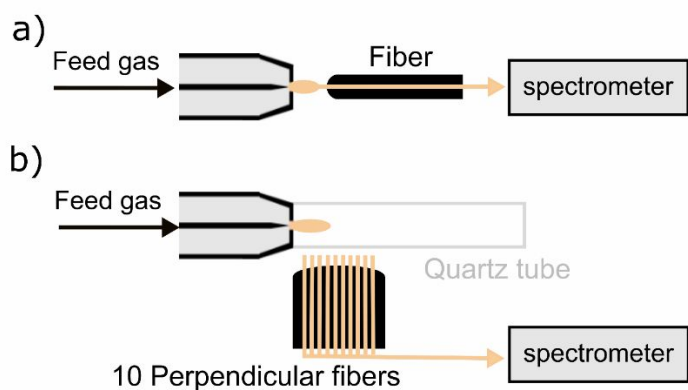
where  $\ln(I^{(v)}/I_0^{(v)})$  is the measured absorbance ( $A(v)$ ) as a function of wavenumber ( $v$ ),  $\sigma_j(v)$  is the absorption cross-section of species  $j$  as a function of  $v$  [in cm<sup>2</sup> molecule<sup>-1</sup>], and  $L$  is the length of the absorbance pathway [in cm]. The last term in the brackets performs the unit conversion from (cm<sup>-3</sup>) to (ppm), where  $n$  is the gas density at 323 Kelvin (the temperature in the gas cell). This method is commonly used in gas analysis using FTIR.<sup>3-5</sup> Though for NO, NO, NO<sub>2</sub> and N<sub>2</sub>O the concentration was determined through both Beer's law and the Bruker system, all concentrations reported are determined using Beer's law, for consistency.

Figure S1 shows the theoretical absorbance peaks for NO, NO<sub>2</sub>, N<sub>2</sub>O, NH<sub>3</sub>, HNO<sub>3</sub>, HNO<sub>2</sub> and O<sub>3</sub>. Species present in detectable quantities were NO, NO<sub>2</sub>, NH<sub>3</sub> and HNO<sub>2</sub>, though not at all conditions. The concentration of N<sub>2</sub>O was <2 ppm for all conditions measured. HNO<sub>3</sub> was not detected at any of the examined conditions, as well as O<sub>3</sub> due to the relatively high gas temperature of the afterglow.



**Figure S3.** (a) Overview of absorption bands from NO, NO<sub>2</sub>, N<sub>2</sub>O, HNO<sub>3</sub>, HNO<sub>2</sub>, NH<sub>3</sub> and O<sub>3</sub>. (b) HNO<sub>2</sub> and HNO<sub>3</sub> bands in the 3400 – 3800 cm<sup>-1</sup> region. (c) HNO<sub>2</sub>, HNO<sub>3</sub>, NO and NO<sub>2</sub> bands in the 1550 – 1850 cm<sup>-1</sup> region. (d) HNO<sub>2</sub> and HNO<sub>3</sub> bands in the 1100 - 1500 cm<sup>-1</sup> region. (e) HNO<sub>2</sub> and HNO<sub>3</sub> bands in the 700 - 1100 cm<sup>-1</sup> region. All simulated spectra have been taken from the HITRAN database<sup>1</sup>, except for HNO<sub>2</sub> and the HNO<sub>3</sub> region 3700 – 3800 cm<sup>-1</sup> annotated with dashed lines, which were digitized from Pipa et al.<sup>6</sup> based on literature values.<sup>7,8</sup>

#### S4. Experimental setups of OES



**Figure S4.** Basic gas analysis experimental setup as explained in the main text. (a) OES setup axial to the jet. (b) OES setup perpendicular to the afterglow using 10 fibers for spatially resolved measurements (1-10 mm from the nozzle).

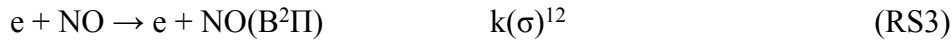
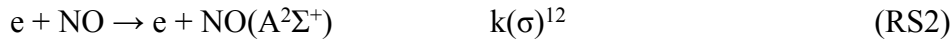
#### S5. Optical emission spectroscopy

NH(A<sup>3</sup>Π–X<sup>3</sup>Σ) can be detected at 336.00 nm; there are no major interferences in this region.

The main pathway for production of  $\text{NH}(\text{A}^3\Pi\text{-X}^3\Sigma)$  is through  $\text{NH}_3$ . It is commonly accepted that  $\text{NH}(\text{A}^3\Pi\text{-X}^3\Sigma)$  is a good indication of the  $\text{NH}_3$  density.<sup>9</sup>



The  $\text{NO}(\text{A}^2\Sigma^+\text{-B}^2\Pi)$  transition was detected at 226.94 nm. The  $\text{NO}(\text{B}^2\Pi\text{-X}^2\Pi)$  transition (around 340 nm<sup>11</sup>) was only observed in the afterglow. Both  $\text{NO}(\text{A}^2\Sigma^+)$  and  $\text{NO}(\text{B}^2\Pi)$  states are formed mainly through:



In order to correlate intensities of excited species measured in OES to ground state densities and to compare different bands with each other, a number of corrections and approximations have to be considered as follows:

- (1) Quenching of excited states is taken into account.
- (2) The measured intensities are corrected for the spectrometer sensitivity and fibre optics transparency.
- (3) The signals are corrected to take into account the difference in excitation probabilities associated with the different transitions used. This means the emission of the excited states can be linked to the emission of the ground state.

These corrections have been made under the assumptions of the corona model approximation (explained in sections S5.1-S5.3 below).

### S5.1. Correction for quenching by $\text{H}_2\text{O}$ , $\text{O}_2$ and $\text{N}_2$

Quenching reduces the fraction of the state that can be observed through photon emission<sup>13</sup> and collisional quenching reduces the effective branching ratio of a spontaneous transition  $i \rightarrow k$ . Following Hartinger et al.<sup>14</sup>, the quenching of the excited species can be expressed as shown in eq. S1. Here  $q$  represents the fraction of the excited species that is present after quenching.

$$q = \frac{A}{A+Q}, \text{ where } Q = \sum n_i v_{ri} \sigma_I \quad (\text{S2})$$

- $A$  Einstein transition coefficient ( $s^{-1}$ )  
 $Q$  effective quenching rate ( $s^{-1}$ )  
 $n_i$  number density of the quenching partner  $i$  ( $cm^{-3}$ )  
 $v_{ri}$  relative velocity ( $cm/s$ )  
 $\sigma_I$  cross section ( $cm^2$ )

In case quenching coefficients instead of cross sections are given,  $Q$  is expressed as follows:

$$Q = \sum n_i k_{iq} \quad (\text{S3})$$

- $k_{iq}$  quenching coefficient ( $cm^3/s$ )

The Einstein transition coefficient denotes the total spontaneous emission rate of the upper level, which is equal to its reciprocal lifetime. For NO(A<sup>2</sup>Σ<sup>+</sup>-<sup>2</sup>Π) A is taken from LIFBASE<sup>15</sup>. For NH(A<sup>3</sup>Π-X<sup>3</sup>Σ) A is taken from Zhou et al.<sup>16</sup> The values are reported in the summary Table S1. Q is a sum over all possible quenchers, taking into account their density.

The relative speed of the quencher to the quenched molecule is calculated as follows:

$$v_{rel} = \sqrt{\frac{8kT}{\pi\mu}} \quad (S4)$$

$$\text{with } \mu = \frac{1}{\frac{1}{m_1} + \frac{1}{m_2}} = \frac{m_1 m_2}{m_1 + m_2} \text{ in (g/particle)} \quad (S5)$$

$$\text{Meaning } m_i = \frac{1}{M_i \cdot N_A} \quad (S6)$$

With:

$$k = 1.380649 \times 10^{-16} \text{ cm}^2 \text{ g} / (\text{s}^2 \text{ K}), \text{ for } v_{rel} \text{ expressed in cm/s.}$$

This also means that

$$k_{iq} = \sigma_i v_{rel} \quad (S7)$$

For both the quenching coefficients and cross-section there are a wide range of values found in literature. In this work the Q values from three sources were calculated and their average was used as the quenching coefficient. The three sets of constants are shown in Table S2.

With q known, the signal corrected for quenching is calculated using eq. 10:

$$I_{measured} = I_{original} \cdot q \quad (S8)$$

*q* fraction of the signal that is visible after quenching

*I<sub>measured</sub>* measured signal

*I<sub>original</sub>* the signal without quenching

**Table S1.** Einstein transitions coefficients of NH(A<sup>3</sup>Π-X<sup>3</sup>Σ) and NO(A<sup>2</sup>Σ<sup>+</sup>)

Einstein transition coefficient A (1/s)		
NO(A <sup>2</sup> Σ <sup>+</sup> - <sup>2</sup> Π)	9.8×10 <sup>5</sup>	<sup>17</sup>
NH( <sup>3</sup> Π- <sup>3</sup> Σ)	1.39×10 <sup>6</sup>	<sup>16</sup>

**Table S2.** The cross sections and rate coefficients for NH(A<sup>3</sup>Π) and NO(A<sup>2</sup>Σ<sup>+</sup>) quenching by N<sub>2</sub>, O<sub>2</sub> and H<sub>2</sub>O as collisional quenchers.

Quencher	Cross section (NH(A <sup>3</sup> Π)) (cm <sup>2</sup> )		Rate coefficient (NO(A <sup>2</sup> Σ <sup>+</sup> )) (cm <sup>3</sup> /s)		
	Set A	Set B	Set C	Set D	Set E

N <sub>2</sub>	$0.1 \times 10^{-16}$	13	$0.0061 \times 10^{-16}$	18	$0.00047 \times 10^{-10}$	19	$0.00065 \times 10^{-10}$	20	$0.00074 \times 10^{-10}$	19
O <sub>2</sub>	$1.5 \times 10^{-16}$	13	$4.3 \times 10^{-16}$	18	$1.47 \times 10^{-10}$	19	$1.46 \times 10^{-10}$	20	$1.59 \times 10^{-10}$	21
H <sub>2</sub> O	$9.8 \times 10^{-16}$	13	$9.8 \times 10^{-16}$	18	$7.71 \times 10^{-10}$	19	$7.8 \times 10^{-10}$	20	$7.58 \times 10^{-10}$	21

### S5.2 Correction for sensitivity

The difference in light collection at different wavelengths was measured and used to correct the NH(A<sup>3</sup>Π – X<sup>3</sup>Σ) and NO(A<sup>2</sup>Σ<sup>+</sup> – <sup>2</sup>Π) band intensities. As a light source, a Hamamatsu D2 model L7293 lamp was used with a C9598 power supply.

### S5.3 Correction for excitation probability

The correction for the excitation probability can be applied under the approximation that the systems behaves as assumed in the corona model. The corona approximation is a simplified approach to population densities in nonequilibrium plasmas. It assumes an equilibrium where transition upwards for ionization and excitation occurs solely through electron impact, and the transitions downwards only occurs through spontaneous emission and radiative decay. As we are working at atmospheric pressure and our averaged temperature is low, this means we do not take into account collisional recombination, 3-body recombination, step-wise excitation, charge exchange, and V-V and V-T processes.<sup>22</sup>

Direct electron impact excitation requires electrons with an energy above 5.48 eV and 3.68 eV, for NO(A<sup>2</sup>Σ<sup>+</sup> – <sup>2</sup>Π) and NH(A<sup>3</sup>Π – X<sup>3</sup>Σ),<sup>23</sup> respectively. The corresponding excitation probability will be different by the following factor (eq. 11):

$$\frac{P(NO)}{P(NH)} = \frac{n_{e > 5.48 \text{ eV}}}{n_{e > 3.68 \text{ eV}}} \times \frac{\exp\left(\frac{EE_{NO}}{k_b \cdot T_e}\right)}{\exp\left(\frac{EE_{NH}}{k_b \cdot T_e}\right)} = 0.17 \times \frac{n_{e > 5.48 \text{ eV}}}{n_{e > 3.68 \text{ eV}}} \quad (S9)$$

- $P$  probability of electron impact excitation
- $n_e$  electron density
- $T_e$  electron temperature
- $k_b$  Boltzmann constant

The ratio of the density of electrons with the required energy for the excitation to NO(A<sup>2</sup>Σ<sup>+</sup>) and NH(A<sup>3</sup>Π) can be presented by the fraction of electrons assuming a Maxwell-Boltzmann energy distribution, which results in an excitation factor of 0.0331 for NO(A<sup>2</sup>Σ<sup>+</sup>) excitation compared to NH(A<sup>3</sup>Π). It has to be noted that the considered corona-model corrected for quenching processes is valid for low ionization degree plasmas with only electron impact excitation mechanisms. Additional excitation processes can lead to overestimation of the excited states density in the corona model. However, a model including a complete set of population processes would require a collisional-radiative model which is not yet available in literature for mixtures such as used in our work.

### S6. NO<sub>x</sub> formation in (humid) N<sub>2</sub> and air

This is a discussion based on the NO and NO<sub>2</sub> trends presented in Figure 2 of the manuscript. Describing the detailed reaction mechanisms for HNO<sub>x</sub>, NO, NO<sub>2</sub> and NH<sub>3</sub>, as well as their interplay, requires dedicated computational studies based on a chemical kinetics model, which can take into account large reaction sets, while incorporating the plasma parameters (e.g., power density) as input. We did this for a much simpler chemical system consisting only of dry air<sup>24</sup>, where we discussed how reverse reactions of the Zeldovich mechanism can be suppressed and the vibrational nonequilibrium can be promoted through the use of pulsed power and resulting pulsed temperature. A complete computational model with added H<sub>2</sub>O would be much more complex, and was outside the scope of the present work. However, based on our general insights obtained from our other models, data from literature, and our present experimental data, we can hypothesize the following mechanisms.

In brief, in humid N<sub>2</sub> the dominating mechanism for NO and NO<sub>2</sub> formation is the extended Zeldovich mechanism (see RS1 in Table S3), as discussed by Gromov et al.<sup>25</sup>, because H<sub>2</sub>O is the sole oxygen source. However, the concentrations of NO and NO<sub>2</sub> were below 1 ppm for the whole range of used H<sub>2</sub>O content (<1-100% relative humidity)), likely because all NO<sub>x</sub> reacted further to form HNO<sub>2</sub>, as seen in Figure 2a and 2b.

On the other hand, in humid air where O<sub>2</sub> is readily available, the NO<sub>x</sub> concentration is not only dramatically higher than in humid N<sub>2</sub> (where NO<sub>x</sub> concentration was <1 ppm), but is up to 4 times higher than the HNO<sub>2</sub> concentration (e.g., 69 ppm HNO<sub>2</sub>, 254 ppm NO<sub>x</sub> at 50% relative humidity and 2 L/min; Figure 2d). In this scenario, NO<sub>x</sub> formation is guided by both the traditional non-thermal (RS2 and RS3) and the extended Zeldovich mechanisms (RS1) shown in Table S3.

**Table S3.** (Extended) Zeldovich reactions, their corresponding reaction rate coefficients and relevant temperature ranges.

Reaction	Rate coefficients <sup>a</sup>	Temperature range	Ref
N + OH → NO + H	$4.7 \times 10^{-17}$	300–2500 K	RS1 <sup>26</sup>
O <sub>2</sub> + N → NO + O	$4.47 \times 10^{-12} \times e^{-27188/RT}$	298–5000 K	RS2 <sup>26</sup>
N <sub>2</sub> + O → NO + N	$3.01 \times 10^{-10} \times e^{-318000/RT}$	1400–4000 K	RS3 <sup>26</sup>

<sup>a</sup> Unit: cm<sup>3</sup>/(molecules·s) for two-body reactions, and cm<sup>6</sup>/(molecules<sup>2</sup>·s) for three-body reactions. T is the gas temperature.

### S7. OES spectra recorded perpendicular to the plasma effluent

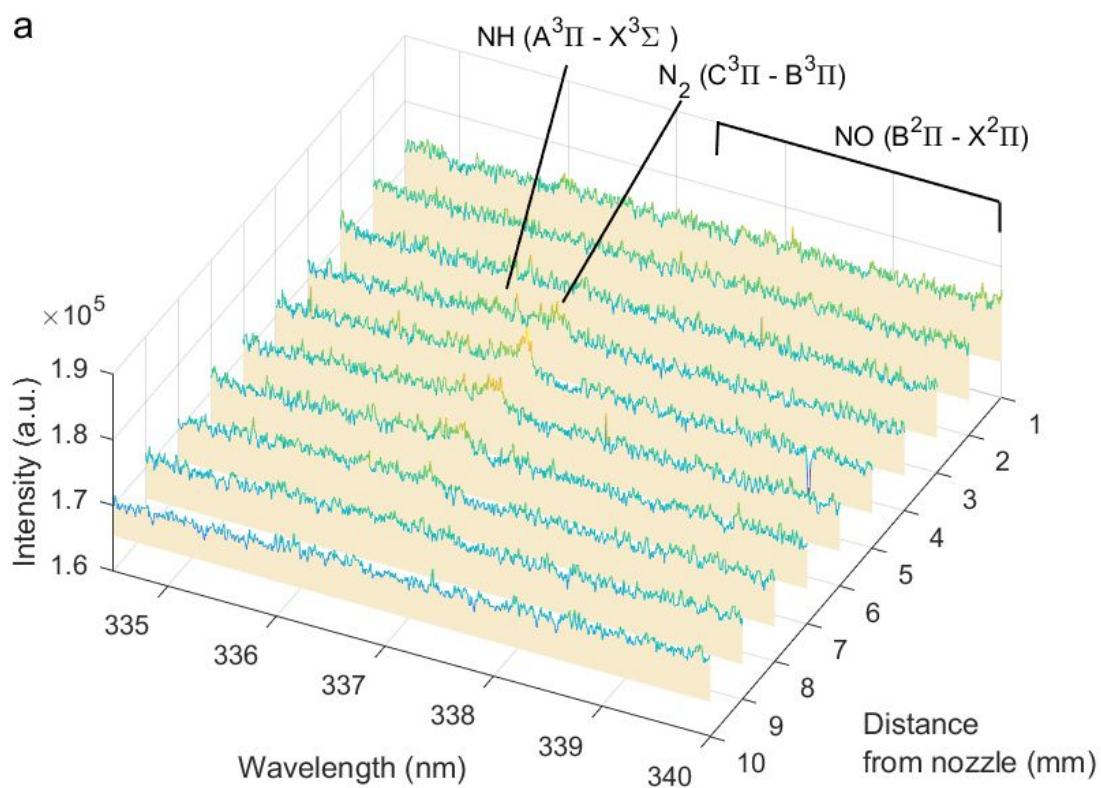
**Table S4.** Overview of the waterfall plot conditions and their respective Figure numbers.

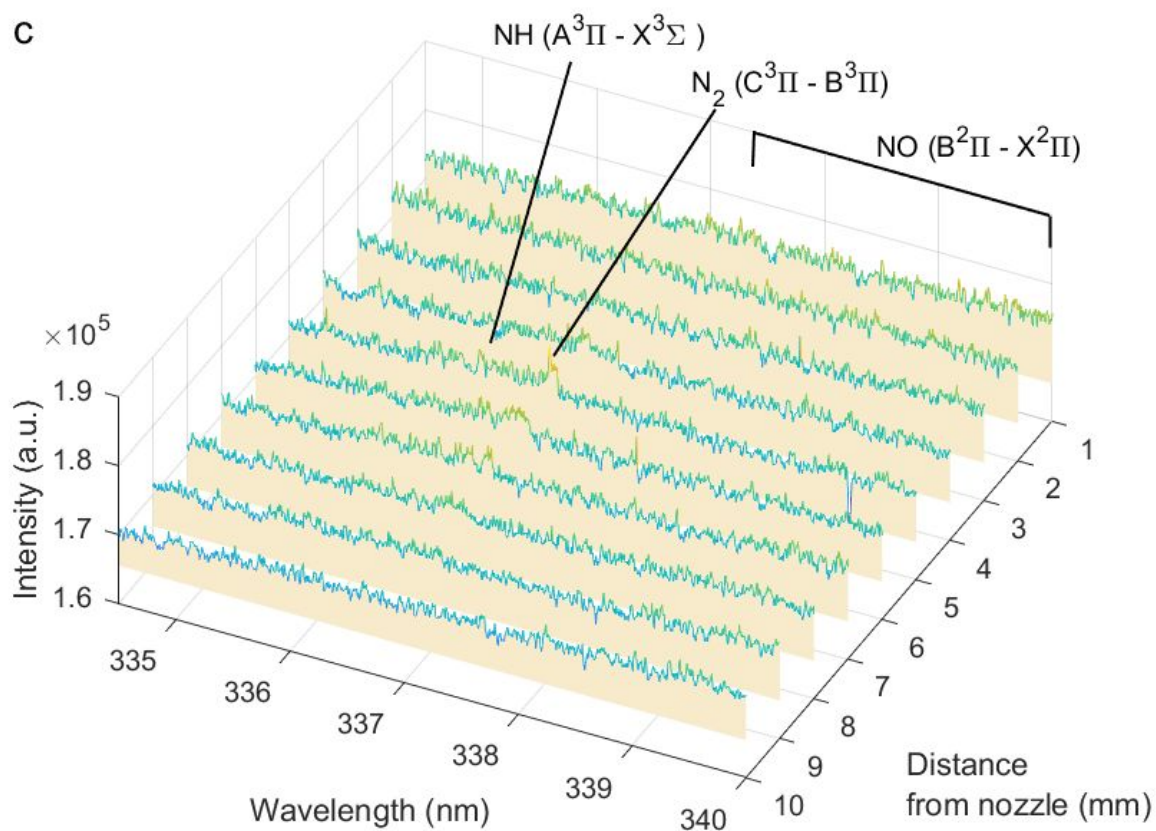
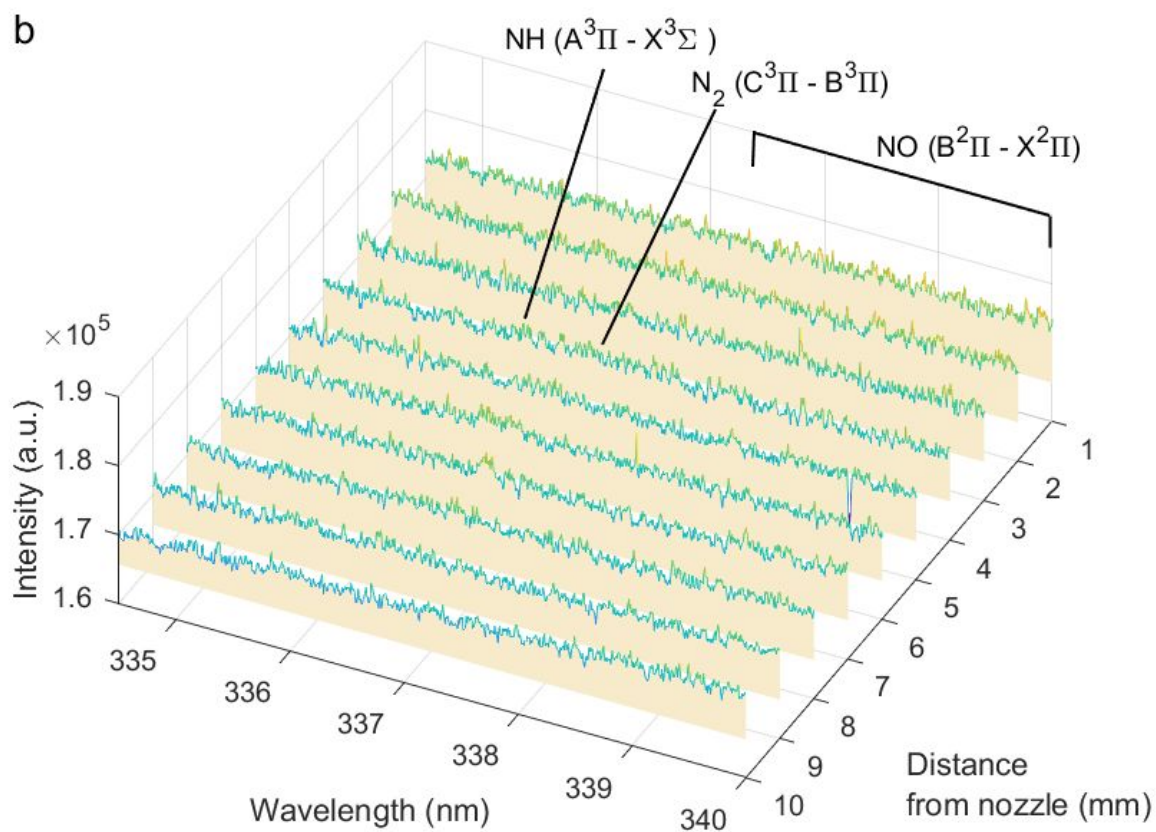
Gas	Air									
Flow rate (Slm)	0.5					2				
Relative humidity at 20°C (%)	<1	5	30	50	100	<1	5	30	50	100
<b>Figure S4.</b>	<b>a</b>	<b>b</b>	<b>c</b>	<b>d</b>	<b>e</b>	<b>f</b>	<b>g</b>	<b>h</b>	<b>i</b>	<b>j</b>
Gas	N <sub>2</sub>									
Flow rate (Slm)	0.5					2				

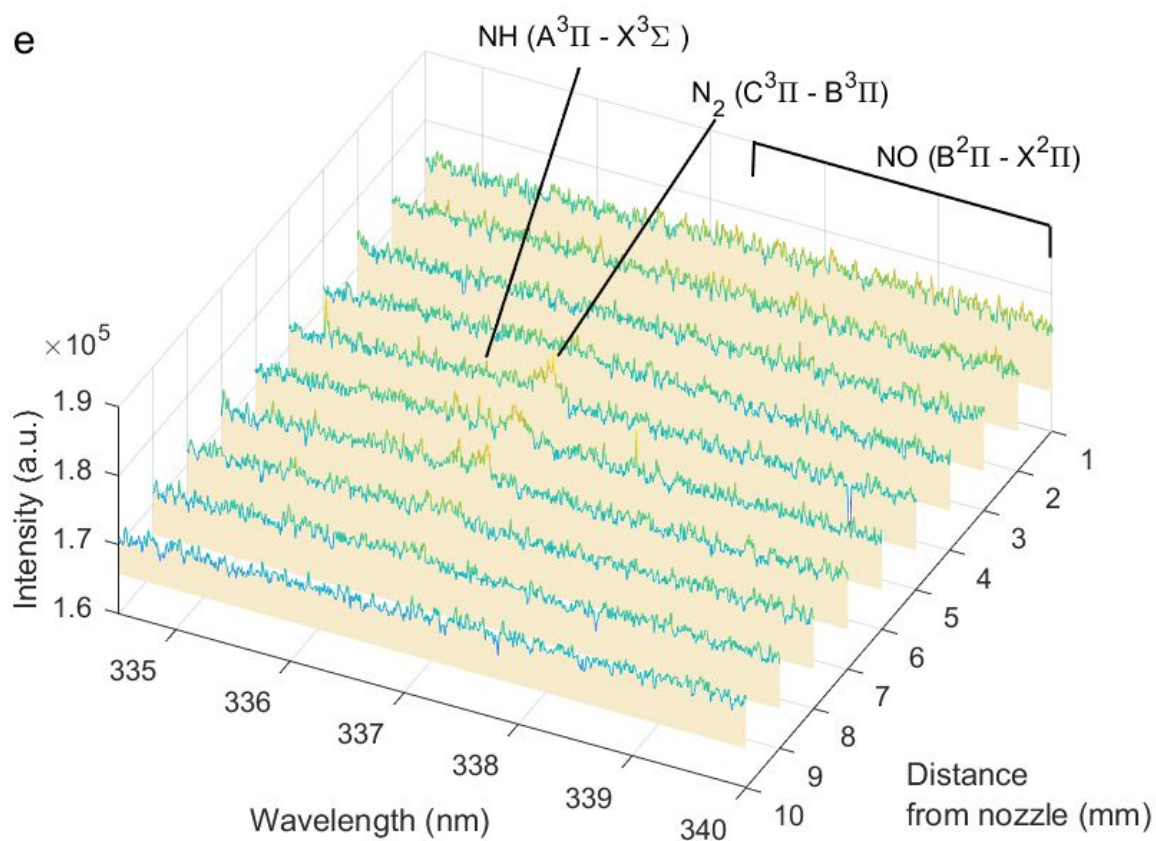
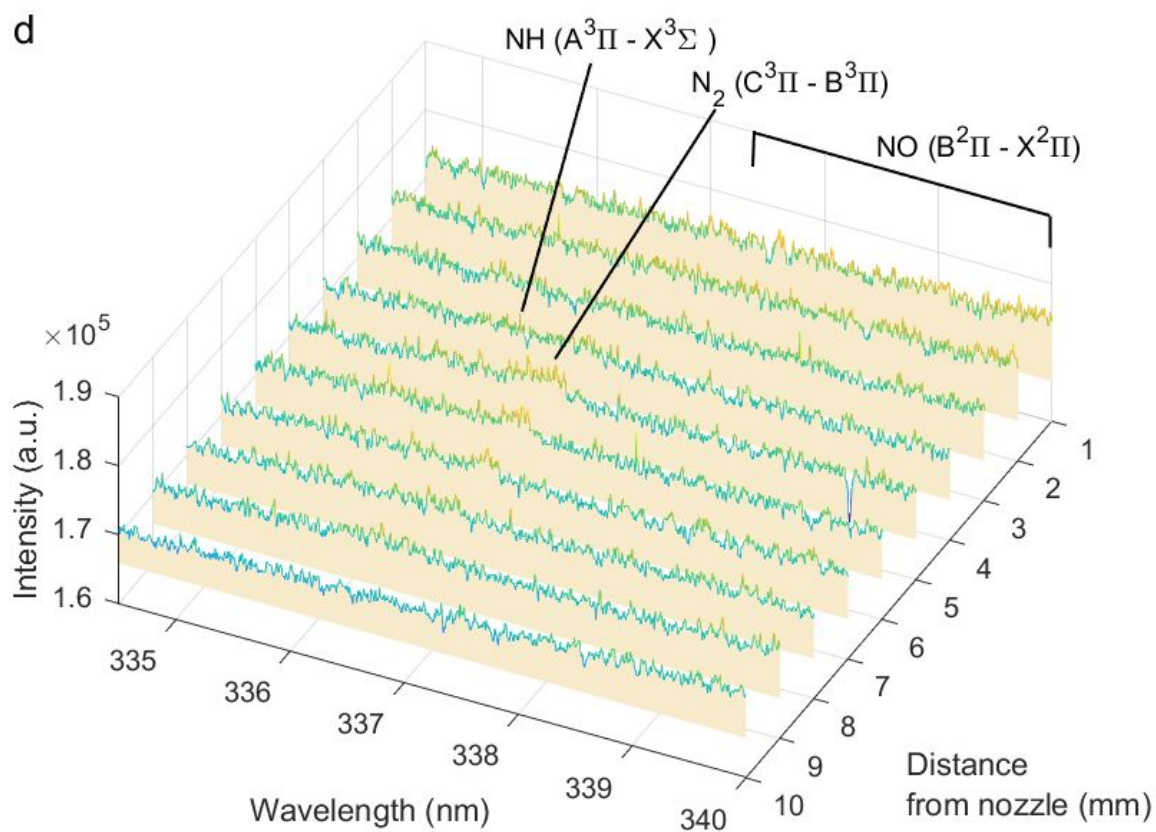
Relative humidity at 20°C (%)	<1	5	30	50	100	<1	5	30	50	100
<b>Figure S4.</b>	<b>k</b>	<b>l</b>	<b>m</b>	<b>n</b>	<b>o</b>	<b>p</b>	<b>q</b>	<b>r</b>	<b>s</b>	<b>t</b>

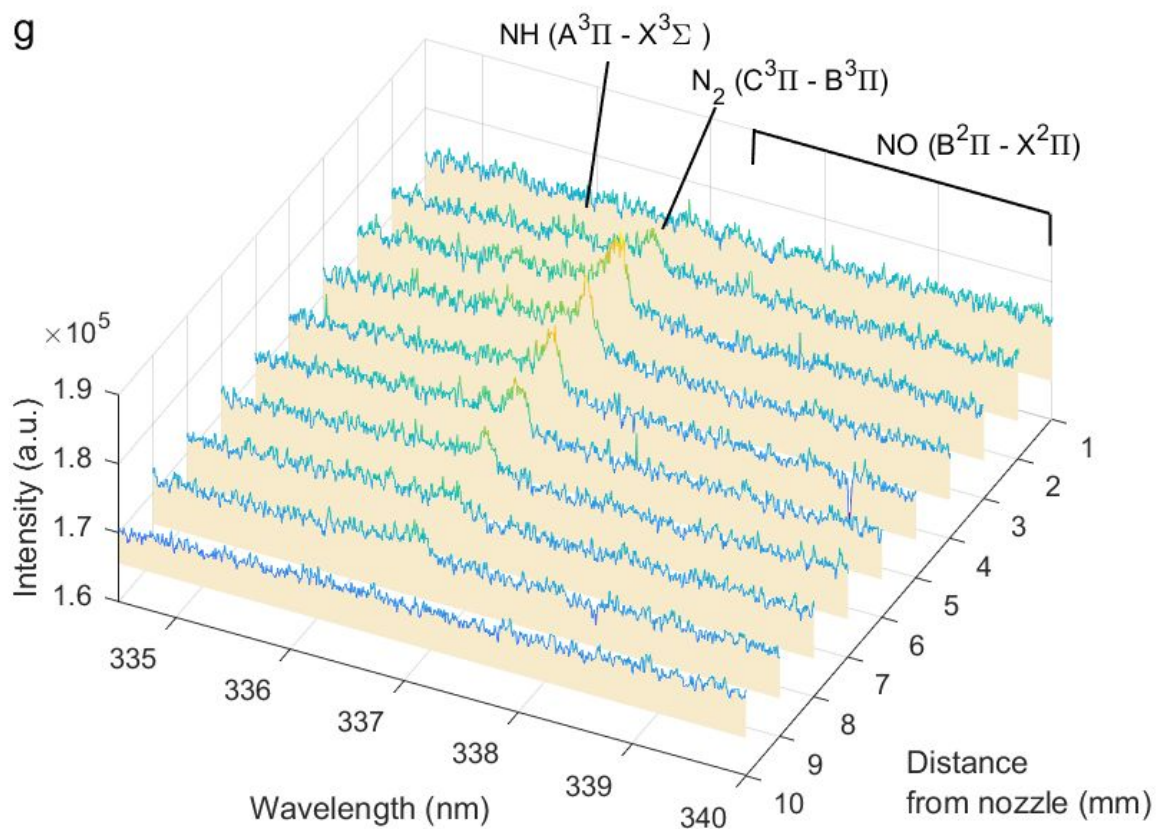
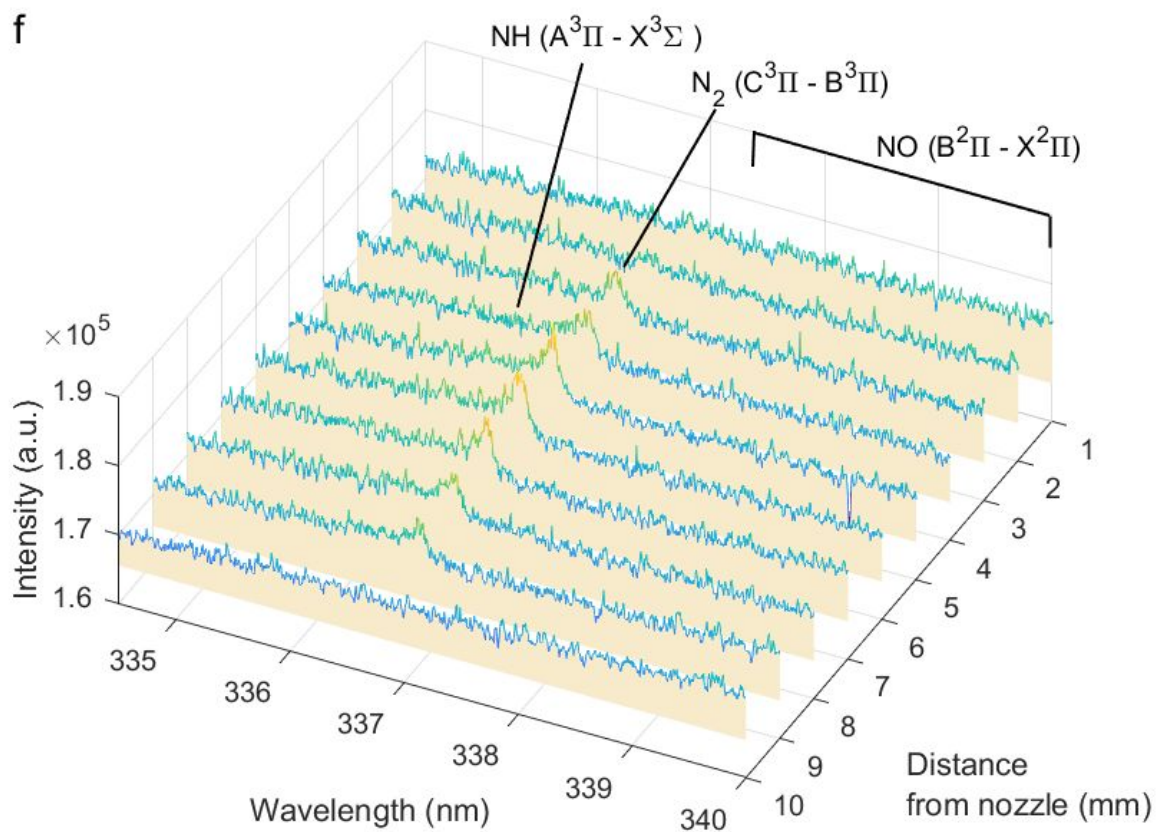


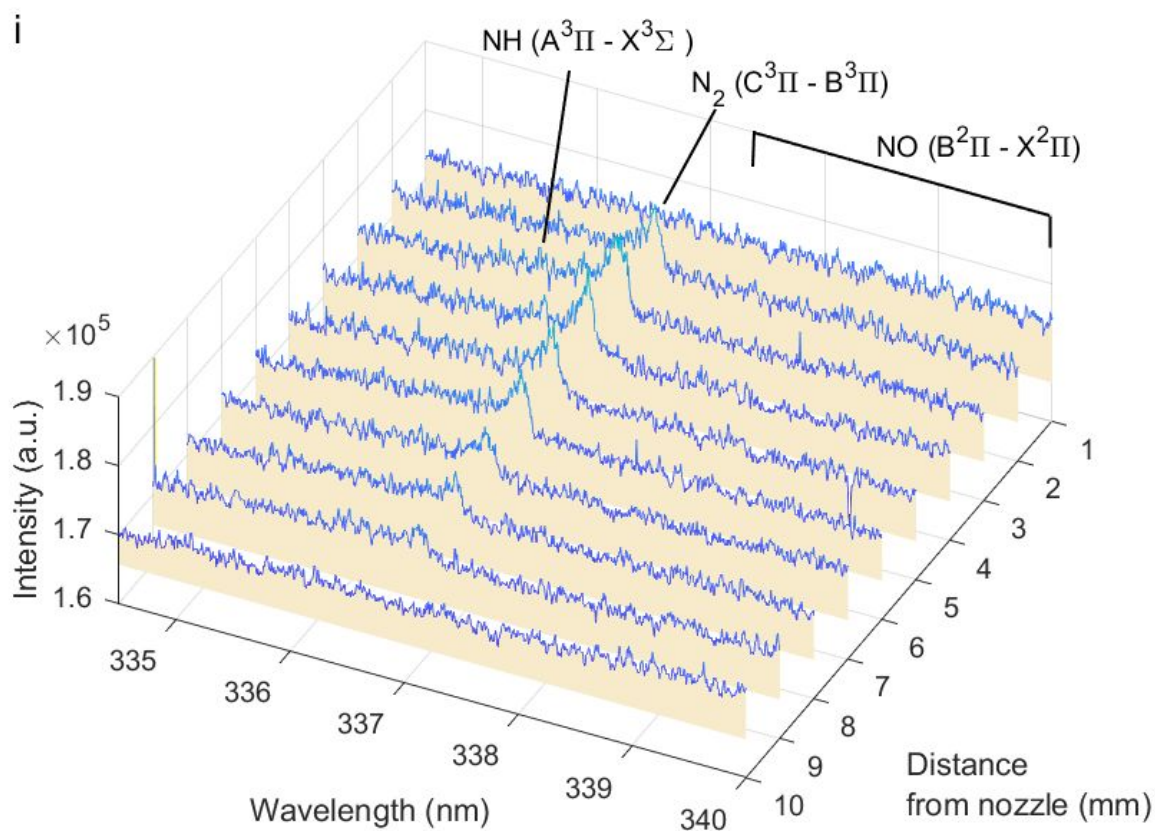
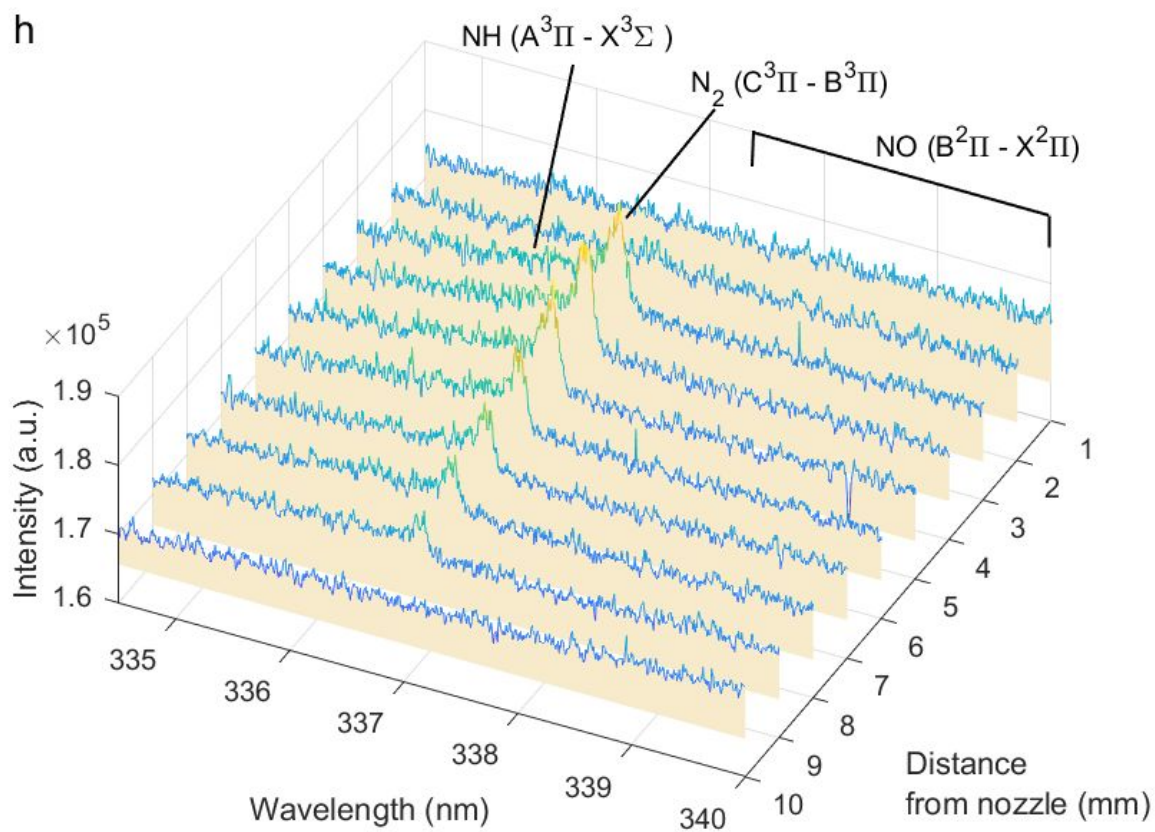
**Figure S5.** Emission spectra (334–340 nm) as a function of the distance from the jet nozzle (1–10 mm). The full list of the experimental conditions (Figures S5a – S5t) is shown in Table S3 above.

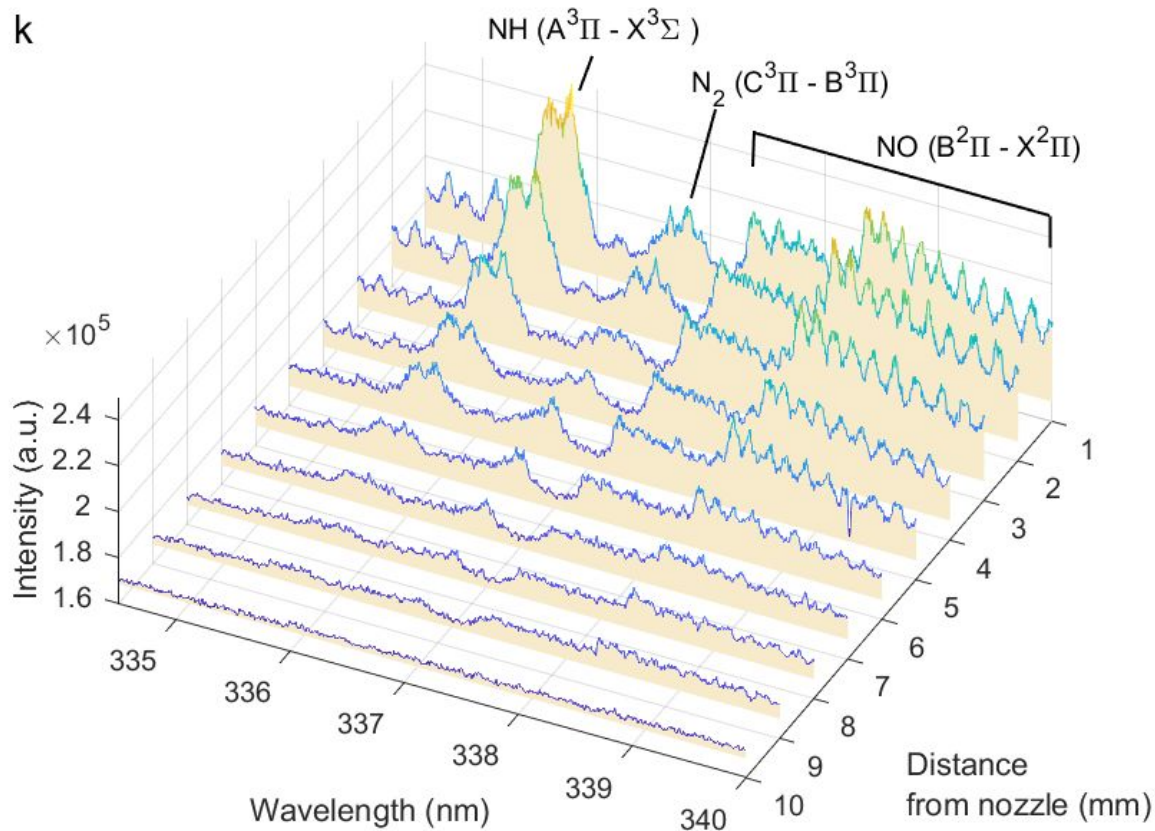
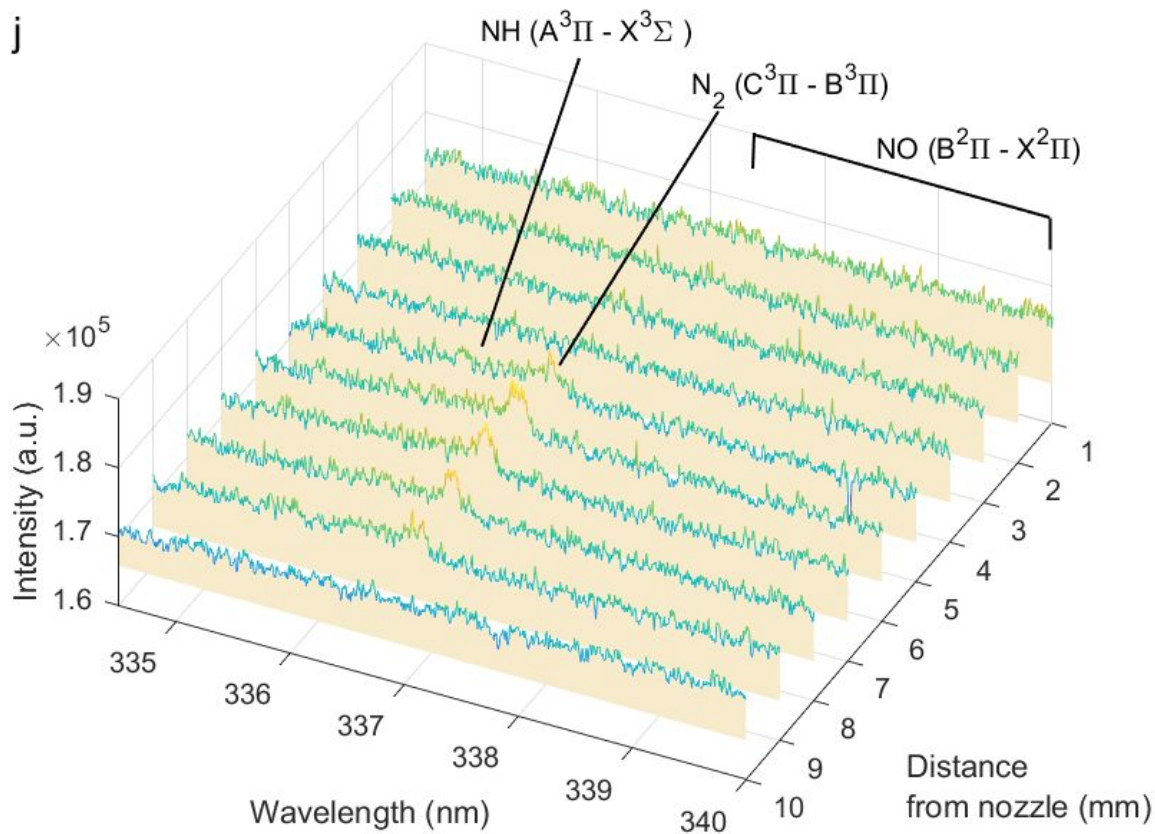


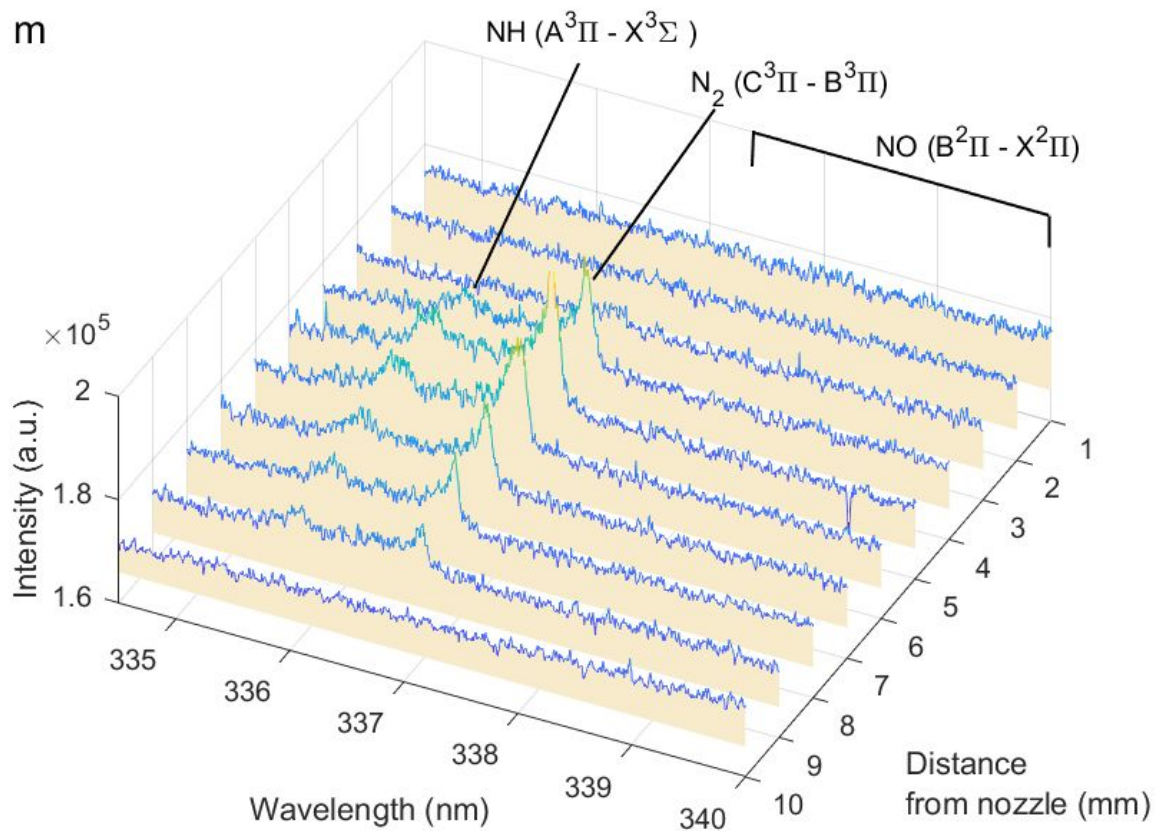
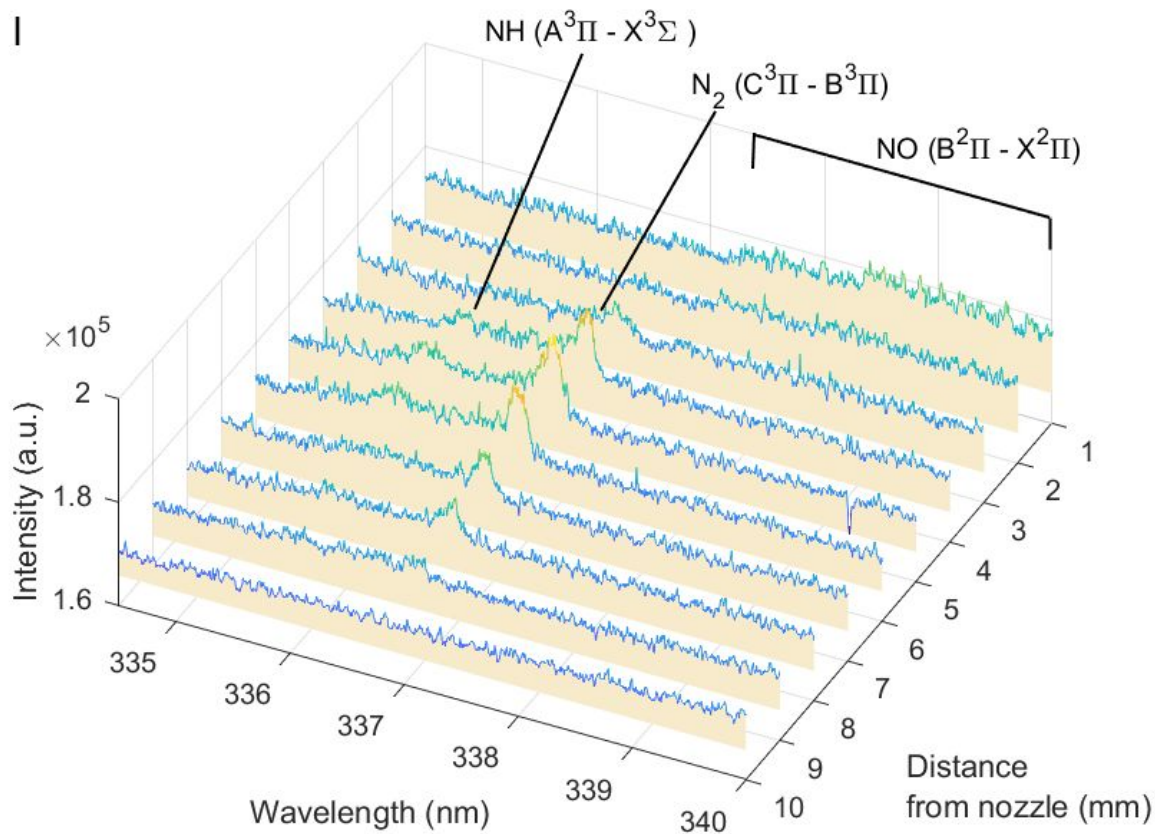


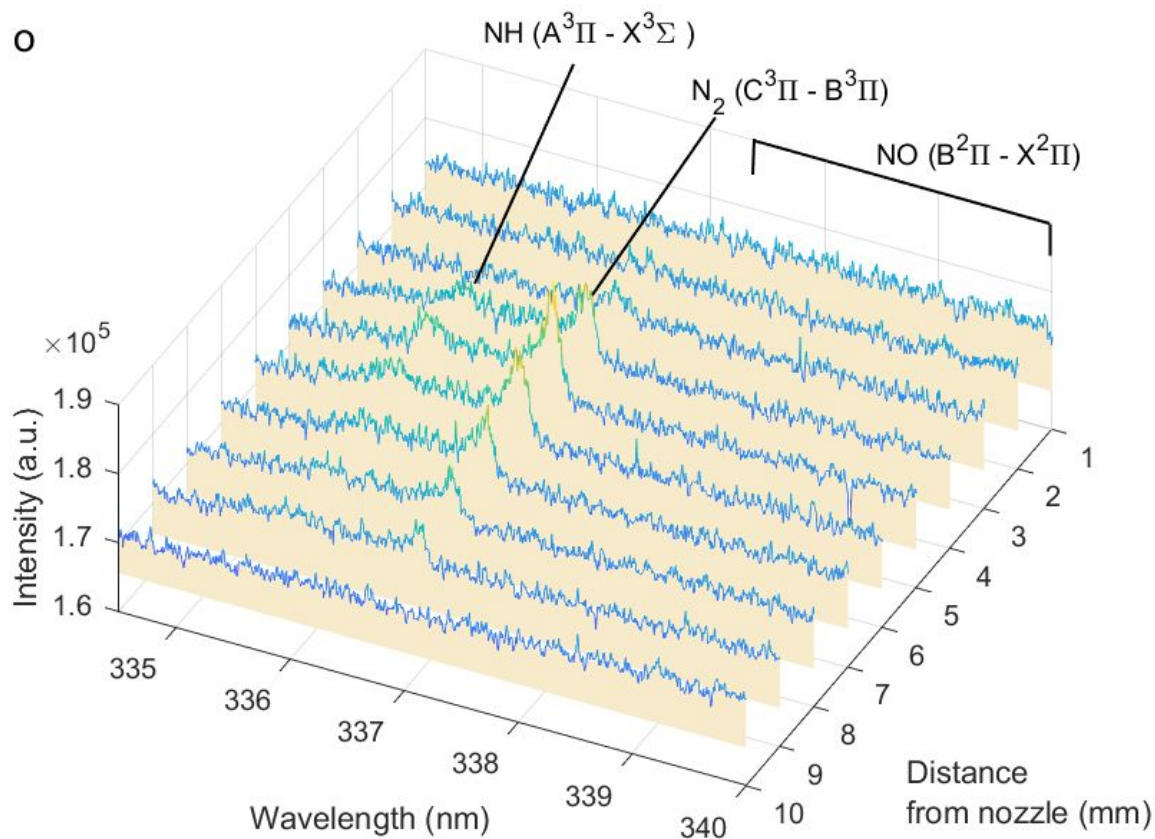
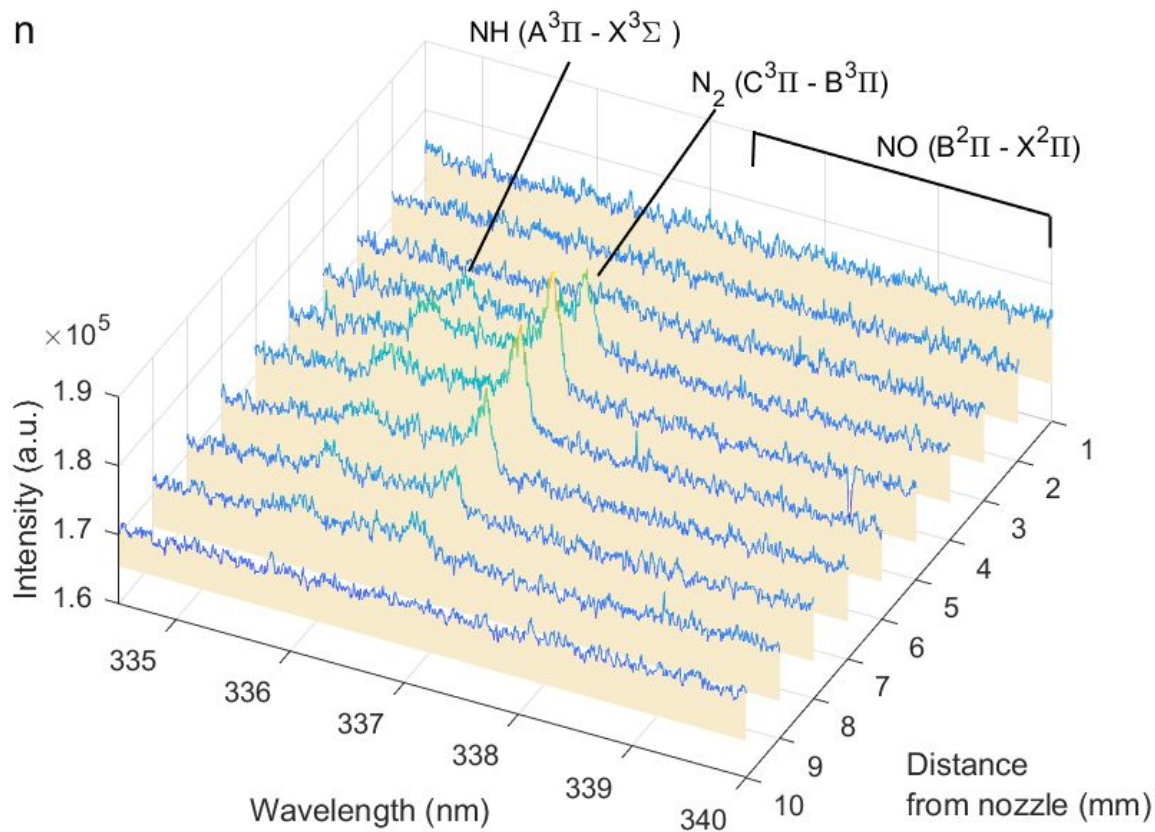




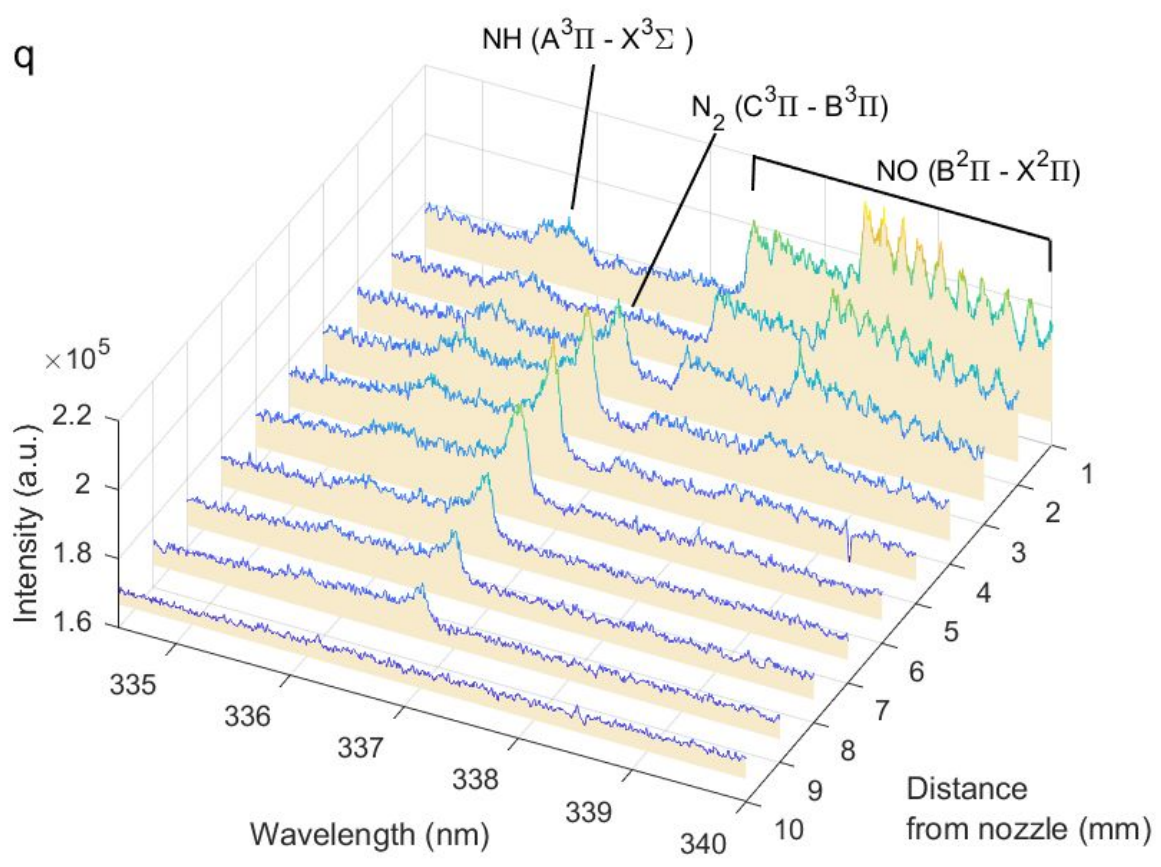
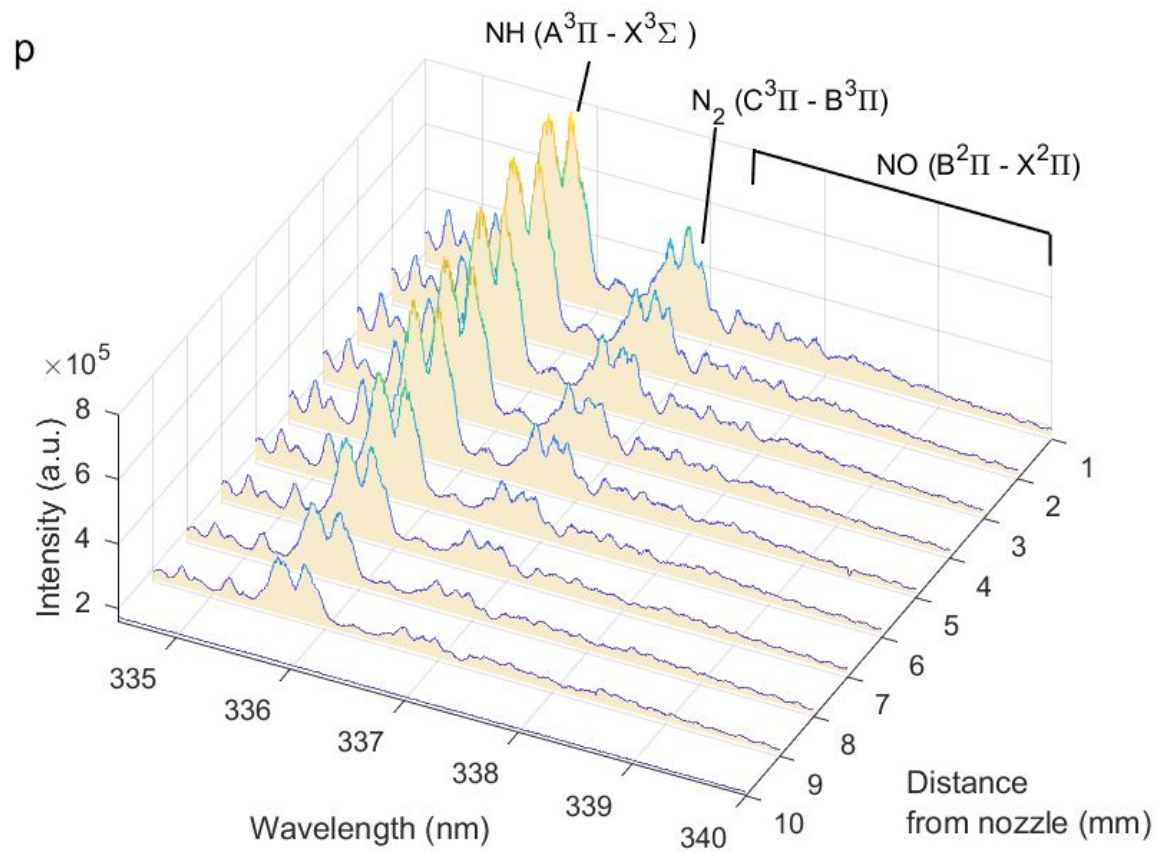


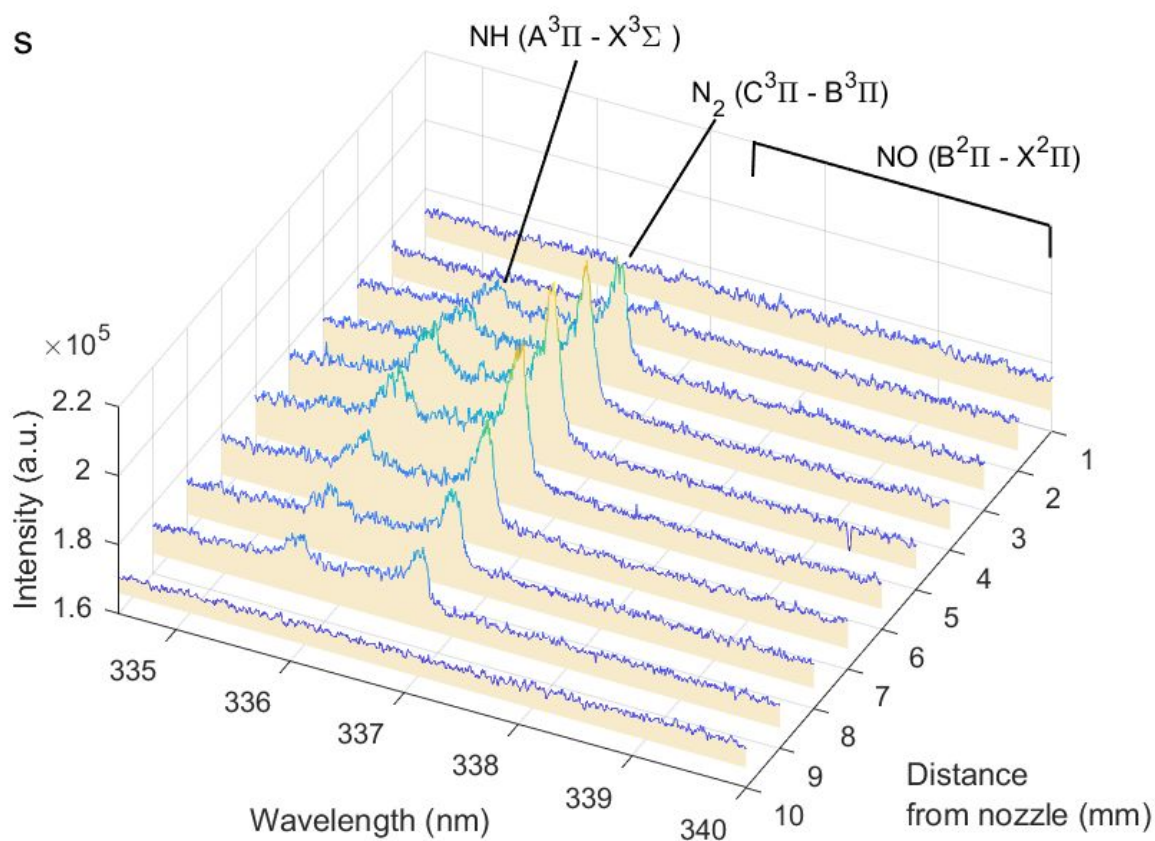
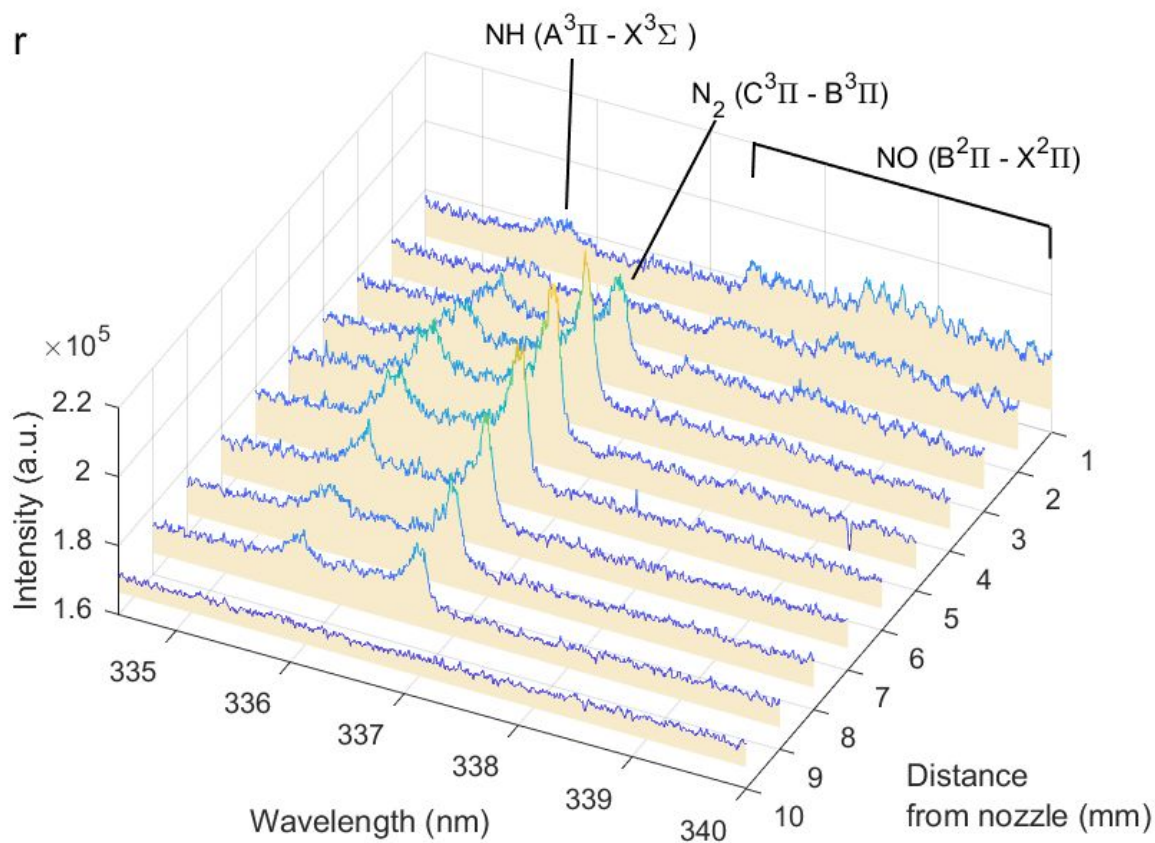


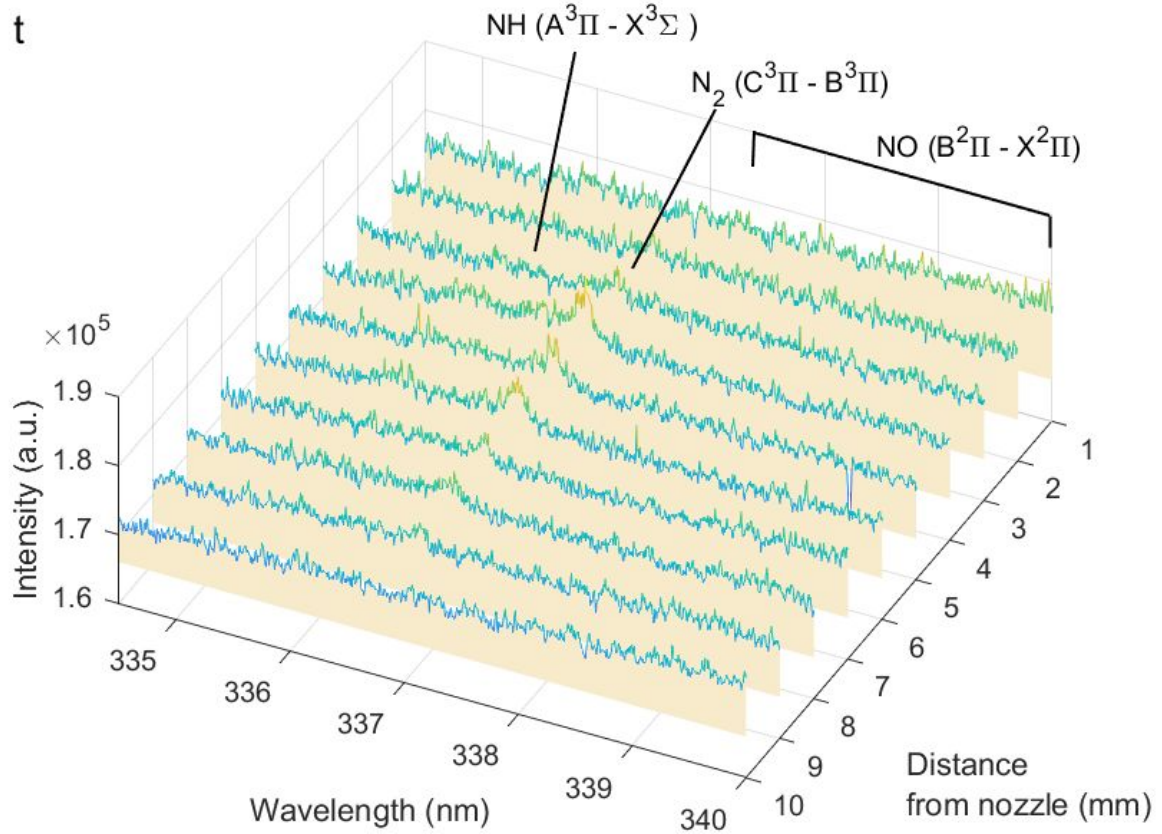












### S8. Energy consumption and production rate

Using the plasma power ( $P$ ) and the total (H)NO<sub>x</sub> concentration, the EC was calculated according to eq. 12. The EC is expressed in MJ/(mol N), where mol N is the amount of nitrogen fixed. The power was close to constant for all conditions, as discussed in detail elsewhere<sup>24,27</sup>, hence in the first approximation the same plug power (1.04 W) was used for all conditions.

$$\begin{aligned}
 EC \left( \frac{MJ}{mol N} \right) &= \frac{P(W)}{\text{mol of (H)NO}_x \text{ produced per second} \left( \frac{mol}{s} \right)} \times \frac{1}{10^6 \left( \frac{J}{MJ} \right)} \\
 &= \frac{P(W) \times 10^6 \times 60 \left( \frac{s}{min} \right) \times 22.4 \left( \frac{L}{mol} \right)}{(C_{HNO_2} + C_{NO_2} + C_{NO} + C_{NH_3}) \text{ (ppm)} \times \text{Flowrate} \left( \frac{L}{min} \right) \times 10^6 \left( \frac{J}{MJ} \right)} \quad (S10)
 \end{aligned}$$

The detailed methodology of energy consumption calculations is given in our previous work.<sup>24</sup> It has to be emphasized here that for clarity of the results we only report the total energy consumption, which can be drastically improved by optimization of the power supply system. As shown in our previous results, both experimentally and numerically, the plasma power

which is used to support the sustaining of the discharge, can be a factor of magnitude lower than the total power. The engineering challenge is to design a power system where power efficiency is optimized which is however out of the scope of our current research. Note that the values of the plasma EC look much better, i.e., with values of 0.42 MJ/(mol N fixed)<sup>24</sup>, but they don't account for the power supply efficiency, and for real application, the total EC should be considered.

As seen from the data, even the lowest EC we observed is still ca. 4 times higher than the EC of Haber-Bosch, which is 0.48 MJ/(mol N). Nonetheless, plasma has the advantage of being able to use renewable electricity, because of its fast switch on/off capacity, and is therefore promising for distributed fertilizer production. We infer that plasma processes should be used as an auxiliary technology, rather than substituting the current industrial state-of-the-art entirely.

**Table S5.** Average energy consumption (EC) of nitrogen fixation.

Flow rate (L/min)	Relative Humidity (%)	EC (MJ/(mol N fixed))	
		Air	N <sub>2</sub>
0.5	<0.1	5.54	-
	5	5.40	238.01
	30	5.03	192.28
	50	4.79	78.25
	100	6.12	59.22
	2	<0.1	4.45
2	5	3.37	106.03
	30	2.93	43.13
	50	2.18	22.03
	100	2.70	60.76

The production rate (PR) of the various products (x), and the conversion of N<sub>2</sub> in our system was calculated as shown in eq. 13 and 14:

$$PR_x \left( \frac{mg}{h} \right) = \frac{C_x \text{ (ppm)} \times \text{Flow rate} \left( \frac{L}{min} \right) \times 60 \left( \frac{min}{h} \right)}{22.4 \left( \frac{L}{mol} \right) \times 10^3} \times M_x \left( \frac{g}{mol} \right) \quad (S11)$$

$$N_2 \text{ conversion (\%)} = \frac{(C_{HNO_2} + C_{NO_2} + C_{NO} + C_{NH_3}) \text{ (ppm)}}{N_2 \text{ fraction in the feed gas (ppm)} \times 2} \times 100\% \quad (S12)$$

**Table S6.** Average production rate (PR) of the products of nitrogen fixation, and the conversion of N<sub>2</sub>

Flow Rate (L/min)	Relative Humidity (%)	PR (mg/h)								N <sub>2</sub> conversion (%)	
		Air				N <sub>2</sub>				Air	N <sub>2</sub>
		NO	NO <sub>2</sub>	NH <sub>3</sub>	HNO <sub>2</sub>	NO	NO <sub>2</sub>	NH <sub>3</sub>	HNO <sub>2</sub>		
0.5	<0.1	18	3.4	-	-	-	-	-	-	0.032	-
	5	17	2.7	-	1.8	-	-	0.20	0.19	0.032	0.00059
	30	18	2.7	-	4.2	-	-	0.14	0.53	0.035	0.00073
	50	19	2.9	-	4.0	-	-	0.21	1.3	0.037	0.0018
	100	15	1.7	-	3.5	-	-	0.21	2.39	0.029	0.0024
2	<0.1	19	9.9	-	0.0	-	-	0.00	0.00	0.010	-
	5	23	11	-	5.1	-	-	0.51	0.26	0.013	0.00033
	30	23	11	-	14	-	-	0.92	1.5	0.015	0.00081
	50	37	6.1	-	17	-	-	0.76	4.2	0.020	0.0016
	100	29	5.3	-	15	-	-	0.00	2.9	0.016	0.00058

We note that the EC and PR values shown are not compensated for the losses due to the NH<sub>4</sub>NO<sub>2</sub> decomposition and NH<sub>4</sub>NO<sub>3</sub> precipitation because the experiments with the alkaline washer were not performed for every condition used.

#### REFERENCES

- (1) Gordon, I. E.; Rothman, L. S.; Hargreaves, R. J.; Hashemi, R.; Karlovets, E. v.; Skinner, F. M.; Conway, E. K.; Hill, C.; Kochanov, R. v.; Tan, Y.; Wcisło, P.; Finenko, A. A.; Nelson, K.; Bernath,

- P. F.; Birk, M.; Boudon, V.; Campargue, A.; Chance, K. v.; Coustenis, A.; Drouin, B. J.; Flaud, J. M.; Gamache, R. R.; Hodges, J. T.; Jacquemart, D.; Mlawer, E. J.; Nikitin, A. v.; Perevalov, V. I.; Rotger, M.; Tennyson, J.; Toon, G. C.; Tran, H.; Tyuterev, V. G.; Adkins, E. M.; Baker, A.; Barbe, A.; Canè, E.; Császár, A. G.; Dudaryonok, A.; Egorov, O.; Fleisher, A. J.; Fleurbaey, H.; Foltynowicz, A.; Furtenbacher, T.; Harrison, J. J.; Hartmann, J. M.; Horneman, V. M.; Huang, X.; Karman, T.; Karns, J.; Kass, S.; Kleiner, I.; Kofman, V.; Kwabia-Tchana, F.; Lavrentieva, N. N.; Lee, T. J.; Long, D. A.; Lukashchuk, A. A.; Lyulin, O. M.; Makhnev, V. Y.; Matt, W.; Massie, S. T.; Melosso, M.; Mikhailenko, S. N.; Mondelain, D.; Müller, H. S. P.; Naumenko, O. v.; Perrin, A.; Polyansky, O. L.; Raddaoui, E.; Raston, P. L.; Reed, Z. D.; Rey, M.; Richard, C.; Tóbiás, R.; Sadiq, I.; Schwenke, D. W.; Starikova, E.; Sung, K.; Tamassia, F.; Tashkun, S. A.; vander Auwera, J.; Vasilenko, I. A.; Viganò, A. A.; Villanueva, G. L.; Vispoel, B.; Wagner, G.; Yachmenev, A.; Yurchenko, S. N. The HITRAN2020 Molecular Spectroscopic Database. *J. Quant. Spectrosc. Radiat. Transf.* **2022**, *277*, 107949. DOI 10.1016/j.jqsrt.2021.107949.
- (2) Engeln, R.; Klarenaar, B.; Guaitella, O. Foundations of Optical Diagnostics in Low-Temperature Plasmas. *Plasma Sources Sci Technol* **2020**, *29* (6). DOI 10.1088/1361-6595/ab6880.
  - (3) MacKie, D. M.; Jahnke, J. P.; Benyamin, M. S.; Sumner, J. J. Simple, Fast, and Accurate Methodology for Quantitative Analysis Using Fourier Transform Infrared Spectroscopy, with Bio-Hybrid Fuel Cell Examples. *MethodsX* **2016**, *3*, 128–138. DOI 10.1016/j.mex.2016.02.002.
  - (4) Bacsik, Z.; Mink, J.; Keresztury, G. FTIR Spectroscopy of the Atmosphere. I. Principles and Methods. *Appl. Spectrosc. Rev.* **2004**, *39* (3), 295–363. DOI 10.1081/ASR-200030192.
  - (5) Bacsik, Z.; Mink, J.; Keresztury, G. FTIR Spectroscopy of the Atmosphere Part 2. Applications. *Appl. Spectrosc. Rev.* October 2005, pp 327–390. DOI 10.1080/05704920500230906.
  - (6) Pipa, A. v.; Ropcke, J. Analysis of the Mid-Infrared Spectrum of the Exhaust Gas from an Atmospheric Pressure Plasma Jet (APPJ) Working with an Argon-Air Mixture. *IEEE Trans. Plasma Sci.* **2009**, *37* (6), 1000–1003. DOI 10.1109/TPS.2009.2013865.
  - (7) Cantrell, C. A.; Davidson, J. A.; McDaniel, A. H.; Shetter, R. E.; Calvert, J. G. Infrared Absorption Cross Sections for N<sub>2</sub>O<sub>5</sub>. *Chem. Phys. Lett.* **1988**, *148* (4), 358–363. DOI 10.1016/0009-2614(88)87288-9.
  - (8) Maki, A. G.; Sams, R. L. Diode Laser Spectra of Cis-HONO near 850 Cm<sup>-1</sup> and Trans-HONO near 1700 Cm<sup>-1</sup>. *J. Mol. Struct.* **1983**, *100*, 215–221. DOI 10.1016/0022-2860(83)90093-5.
  - (9) van Duc Long, N.; Al-Bared, M.; Lin, L.; Davey, K.; Tran, N. N.; Pourali, N.; Ken Ostrikov, K.; Rebrov, E.; Hessel, V. Understanding Plasma-Assisted Ammonia Synthesis via Crossing Discipline Borders of Literature: A Critical Review. *Chem. Eng. Sci.* **2022**, *263*, 118097–118110. DOI 10.1016/j.ces.2022.118097.
  - (10) Itikawa, Y. Cross Sections for Electron Collisions with Ammonia. *J. Phys. Chem. Ref. Data* **2017**, *46* (4), 043103–043111. DOI 10.1063/1.5001918.
  - (11) Pearse, R. W. B.; Gaydon, A. G. *Identification of Molecular Spectra*; Chapman & Hall LTD: London, 1950; Vol. Second Edition. DOI 10.1021/ed041pA398
  - (12) Itikawa, Y. Cross Sections for Electron Collisions with Nitric Oxide. *J. Phys. Chem. Ref. Data* **2016**, *45* (3), 033106–033115. DOI 10.1063/1.4961372.

- (13) Buckley, S. G.; Damm, C. J.; Vitovec, W. M.; Anne Sgro, L.; Sawyer, R. F.; Koshland, C. P.; Lucas, D. Ammonia Detection and monitoring with Photofragmentation Fluorescence. *Appl. Opt.* **1998**, *37*, 8382–8391. DOI 10.1364/AO.37.008382.
- (14) Hartinger, K. T.; Nord, S.; Monkhouse, P. B. Quenching of Fluorescence from Na(3 2 P) and K(4 2 P) Atoms Following Photodissociation of NaCl and KCl at 193 Nm. *Appl. Phys. B* **1997**, *64*, 363–367. DOI 10.1007/s003400050185
- (15) J. Luque; D.R. Crosley. LIFBASE: Database and Spectral Simulation Program . SRI International 1999. DOI 10.1063/1.480064
- (16) Zhou, M.; Zhu, Z. Properties of Transitions between X3Σ<sup>-</sup>, A3Π, A1Δ, B1Σ<sup>+</sup>, and C1Π States of NH Radicals. *Comput. Theor. Chem.* **2021**, *1204*, 113458–113468. DOI 10.1016/J.COMPTC.2021.113358.
- (17) Luque, J.; Crosley, D. R. Transition Probabilities and Electronic Transition Moments of the A2Σ<sup>+</sup> - X2Π and D2Σ<sup>+</sup> - X2Π Systems of Nitric Oxide. *J. Chem. Phys.* **1999**, *111* (16), 7405–7415. DOI 10.1063/1.480064.
- (18) Hofzumahaus, A.; Stuhl, F. Electronic Quenching, Rotational Relaxation, and Radiative Lifetime of NH(A3Π, V'=0, N'). *J. Chem. Phys.* **1984**, *82* (7), 3152–3159. DOI 10.1063/1.448213.
- (19) Tamura, M.; Berg, P. A.; Harrington, J. E.; Luque, J.; Jeffries, J. B.; Smith, G. P.; Crosley, D. R. Collisional Quenching of CH(A), OH(A), and NO(A) in Low Pressure Hydrocarbon Flames. *Combust Flame* **1998**, *114* (3–4), 502–514. DOI 10.1016/S0010-2180(97)00324-6.
- (20) Greenblatt, G. D.; Ravishankara, A. R. Collisional Quenching of NO(A, v' =0) by Various Gases. *Chem. Phys. Lett.* **1987**, *136* (6), 501–505. DOI 10.1016/0009-2614(87)80506-7.
- (21) Paul, P. H.; Gray, J. A.; Durant, J. L.; Thoman, J. W. Collisional Electronic Quenching Rates for NO (A2σ<sup>+</sup> v' = 0). *Chem. Phys. Lett.* **1996**, *259*, 508–514. DOI 10.1016/0009-2614(96)00763-4.
- (22) Fantz, U. Basics of Plasma Spectroscopy. *Plasma Sources Sci. Technol.* **2006**, *15* (4), S137–S147. DOI 10.1088/0963-0252/15/4/S01.
- (23) Mo, Y.; Ottinger, C.; Shen, G. Collision-Induced Intersystem Crossing from NH(A1Δ, b 1Σ<sup>+</sup>) to NH(A3Π): Gateway-Mediated and Direct Mechanisms. *J. Chem. Phys.* **1999**, *111* (10), 4598–4612. DOI 10.1063/1.479221.
- (24) Vervloessem, E.; Gorbanev, Y.; Nikiforov, A.; de Geyter, N.; Bogaerts, A. Sustainable NOx Production from Air in Pulsed Plasma: Elucidating the Chemistry behind the Low Energy Consumption †. *Green Chem.* **2022**, *24*, 916–929. DOI 10.1039/d1gc02762j.
- (25) Gromov, M.; Leonova, K.; de Geyter, N.; Morent, R.; Snyders, R.; Britun, N.; Nikiforov, A. N2oxidation Kinetics in a Ns-Pulsed Discharge above a Liquid Electrode. *Plasma Sources Sc. Technol.* **2021**, *30* (6), 65024–65038. DOI 10.1088/1361-6595/abff71.
- (26) Baulch, D. L.; Cobos, C. J.; Cox, R. A.; Frank, P.; Hayman, G.; Just, Th.; Kerr, J. A.; Murrells, T.; Pilling, M. J.; Troe, J.; Walker, R. W.; Warnatz, J. Evaluated Kinetic Data for Combustion Modelling. Supplement I. *J. Phys. Chem. Ref. Data* **1994**, *23*, 847–1033. DOI 10.1063/1.555953.

- (27) Gorbanev, Y.; Vervloessem, E.; Nikiforov, A.; Bogaerts, A. Nitrogen Fixation with Water Vapor by Nonequilibrium Plasma: Toward Sustainable Ammonia Production. *ACS Sust. Chem. Eng.* **2020**, *8*, 2996–3004. DOI 10.1021/acssuschemeng.9b07849.